CMS Draft Analysis Note

2014/01/16
Head Id: 221607
Archive Id: 223252:223253M
Archive Date: 2013/12/19
Archive Tag: trunk

Search for scalar top quark pair production in the dilepton final state at $\sqrt{s} = 8$ TeV with the CMS detector

Drew Baden[1], Javier Brochero[2], Hugues Brun[3], Alicia Calderón[2], Brian Calvert[1], Javier Cuevas[3], Sarah Eno[1], Javier Fernández[3], Santiago Folgueras[3], Ferdinando Giordano[5], Isidro González[3], Alberto Graziano[2], Nick Hadley[1], Ted Kolberg[1], Celso Martínez[2], Jónatan Piedra[3], Ana Rodríguez[2], Manuel Scinta[4], Luca Scodellaro[2], Alessia Tricomi[4], Rocío Vilar[2], Carmen Diez Pardos[6], and Jan Kieseler[6]

[1] University of Maryland
[2] IFCA-CSIC and Universidad de Cantabria
[3] Universidad de Oviedo
[4] INFN and University of Catania
[5] INFN and CSFNSM Catania
[6] DESY

Abstract

We report the results of a search for a scalar partner of the top quark (stop, $\tilde{t}$) using the full dataset of pp collisions at $\sqrt{s} = 8$ TeV collected by the CMS detector. We use a sample of dilepton events ($ee, \mu\mu, e\mu$) with two jets including at least one b-tagged jet to perform the search. The "stransverse mass" (M_{T2}) of the dilepton system with respect to the missing transverse energy is used to separate the stop signal from the dominant $t\bar{t}$ background. The results are interpreted in terms of several simplified models (SMS) which represent possible decays of the stop in R-parity conserving "natural" supersymmetric models where the stop is not the lightest supersymmetric particle.

This box is only visible in draft mode. Please make sure the values below make sense.

PDFAuthor: Ted Kolberg
PDFTitle: Search for scalar top quark pair production in the dilepton final state at sqrt“(s“) = 8 TeV with the CMS detector
PDFSubject: CMS
PDFKeywords: CMS, SUSY, natural SUSY, third generation SUSY

Please also verify that the abstract does not use any user defined symbols

Contents

1 Introduction

Supersymmetry is an extension of the Standard Model which provides a solution to the heirarchy problem by explaining why the Higgs mass can be near the electroweak scale without excessive fine tuning. In models where R-parity is conserved, the lightest supersymmetric particle (LSP) can also provide a candidate for the dark matter observed by astrophysicists. Early LHC data has provided strict limits on the production of generic colored superpartners using final states consisting of jets and missing energy. However, SUSY can still be natural if the superparters of the Higgs, top, and gluon have masses near the electroweak scale. Generic searches may not provide the best limits on these scenarios, so it is necessary to devise new search strategies targeted specifically to the natural scenarios.

This note presents results of a search for scalar top partners produced in pp collisions at a center-of-mass energy of $\sqrt{s} = 8$ TeV. We use events with two opposite-sign high-p_{T} isolated leptons, and two jets with at least one b-tagged jet to perform the search. The stransverse mass variable M_{T2} [1] is used to separate the stop signal from the Standard Model background, which consists primarily of $t\bar{t}$ production.

The stransverse mass is a generalization of the transverse mass M_T to a system of pair produced particles which decay semi-invisibly. In the case of W boson production, M_T is formed from the transverse momentum of a high p_{T} lepton from the W decay and the missing transverse momentum ($E_{\mathrm{T}}^{\mathrm{miss}}$) in the event, which is assumed to come from the corresponding neutrino.

$$M_T = \sqrt{2E_\ell E_{\mathrm{T}}^{\mathrm{miss}}\,[1-\cos(\Delta\phi)]} \tag{1}$$

where $\Delta\phi$ is the angle between lepton and $E_{\mathrm{T}}^{\mathrm{miss}}$ in the transverse plane. Equation 1 shows the definition of M_T in the limit where the masses of the daughter particles can be neglected. It has the property that if the lepton and the $E_{\mathrm{T}}^{\mathrm{miss}}$ both come from the decay of a single particle with mass m, then $M_T \leq m$. In order to generalize to a system with two particles of the same mass, each decaying semi-invisibly, we have to decompose the measured $E_{\mathrm{T}}^{\mathrm{miss}}$ into a sum of two missing transverse momentum vectors as in Equation 2:

$$\mathbf{p}_T^{miss} = \mathbf{p}_{T1}^{miss} + \mathbf{p}_{T2}^{miss}. \tag{2}$$

We may then pair each missing transverse momentum vector with the visible products of the decay in order to form M_T for each half of the pair production. However, since the correct division of the $E_{\mathrm{T}}^{\mathrm{miss}}$ into two components is not known, an alternative is to minimize the maximum of the two transverse masses formed under all possible combinations satisfying Equation 2. That is, we explore the parameter space of all possible hypothetical neutrino momenta that satisfy Equation 2 and for each point in this parameter space we calculate M_T for each half of the event and report the maximum of the two. We take the M_{T2} value for the event to be the minimum of the larger M_T value for each such point. This can be represented by the expression for M_{T2} given in Equation 3:

$$M_{T2}^2 = \min_{\mathbf{p}_{T1}^{miss}+\mathbf{p}_{T2}^{miss}=\mathbf{p}_T^{miss}} \left(\max\left[m_T^2(\mathbf{p}_T^{\ell 1}, \mathbf{p}_{T1}^{miss}), m_T^2(\mathbf{p}_T^{\ell 2}, \mathbf{p}_{T2}^{miss}) \right] \right) \tag{3}$$

It can be shown [1] that this definition of M_{T2} has the same convenient property as the transverse mass: it must be less than the mass of the pair-produced semi-invisbly decaying particle.

In the case of stop searches in the dilepton channel, the primary challenge comes from separating SM $t\bar{t}$ production from the signal, since the composition of the final states is identical except for invisible particles. In dileptonic $t\bar{t}$ events the final state is

$$pp \to t + \bar{t} + X \to bW^+ + \bar{b}W^- + X \to b\ell\bar{\nu}_\ell + \bar{b}\bar{\ell}\nu_\ell + X.$$

Assuming that the contribution of the other products X to the $E_{\mathrm{T}}^{\mathrm{miss}}$ is not large, the assumptions made in the definition of M_{T2} hold for the lepton-$E_{\mathrm{T}}^{\mathrm{miss}}$ system and its value has an upper bound at the W mass. On the other hand, stop pair production events with a dileptonic final state will have at least four invisible particles so long as lepton number and R-parity are both conserved. The stop decays can proceed differently depending on the model considered but a typical example for the models used here is

$$pp \to \tilde{t} + \bar{\tilde{t}} + X \to \bar{\chi}_0 t + \chi_0 \bar{t} + X \to \bar{\chi}_0 bW^+ + \chi_0 \bar{b}W^- + X \to \bar{\chi}_0 b\ell\bar{\nu}_\ell + \chi_0 \bar{b}\bar{\ell}\nu_\ell + X.$$

with χ_0 represnting the lightest supersymmetric particle. Now there are two invisible particles on each side of the decay, and so the partition of the $E_{\mathrm{T}}^{\mathrm{miss}}$ into two components no longer has an upper bound at the W mass.

Sample	Dataset path
Drell-Yan	DYJetsToLL_M-10To50filter_8TeV-madgraph DYJetsToLL_M-50_TuneZ2Star_8TeV-madgraph-tarball DY1JetsToLL_M-50_TuneZ2Star_8TeV-madgraph DY2JetsToLL_M-50_TuneZ2Star_8TeV-madgraph DY2JetsToLL_M-50_TuneZ2Star_8TeV-madgraph DY3JetsToLL_M-50_TuneZ2Star_8TeV-madgraph DY4JetsToLL_M-50_TuneZ2Star_8TeV-madgraph
$Z+\gamma$	ZGToLLG_8TeV-madgraph
$W+\gamma$	WGToLNuG_TuneZ2star_8TeV-madgraph-tauola
W	WJetsToLNu_TuneZ2Star_8TeV-madgraph-tarball
$t\bar{t}$	TT_CT10_TuneZ2star_8TeV-powheg-tauola TT_CT10_TuneZ2star_8TeV-powheg-tauola TTJets_MassiveBinDECAY_TuneZ2star_8TeV-madgraph-tauola TT_8TeV-mcatnlo TTJets_FullLeptMGDecays_8TeV-madgraph-tauola TTJets_FullLeptMGDecays_8TeV-madgraph TTJets_SemiLeptMGDecays_8TeV-madgraph TTJets_HadronicMGDecays_8TeV-madgraph
single t	T_t-channel_TuneZ2star_8TeV-powheg-tauola Tbar_t-channel_TuneZ2star_8TeV-powheg-tauola T_s-channel_TuneZ2star_8TeV-powheg-tauola Tbar_s-channel_TuneZ2star_8TeV-powheg-tauola
tW	TToDilepton_tW-channel-DR_8TeV-powheg-tauola TBarToDilepton_tW-channel-DR_8TeV-powheg-tauola
WW	WWJetsTo2L2Nu_TuneZ2star_8TeV-madgraph-tauola
WW (gluon fusion)	GluGluToWWTo4L_TuneZ2star_8TeV-gg2ww-pythia6
WW	WZ_TuneZ2star_8TeV_pythia6_tauola
ZZ	ZZ_TuneZ2star_8TeV_pythia6_tauola
H_{125}	GluGluToHToWWTo2LAndTau2Nu_M-125_8TeV-powheg-pythia6 VBF_HToWWTo2LAndTau2Nu_M-125_8TeV-powheg-pythia6 GluGluToHToZZTo4L_M-125_8TeV-powheg-pythia6
"Rare"	WZ_TuneZ2star_8TeV_pythia6_tauola GluGluToHToWWTo2LAndTau2Nu_M-125_8TeV-powheg-pythia6 VBF_HToWWTo2LAndTau2Nu_M-125_8TeV-powheg-pythia6 GluGluToHToZZTo4L_M-125_8TeV-powheg-pythia6 WWGJets_8TeV-madgraph WZZNoGstarJets_8TeV-madgraph ZZZNoGstarJets_8TeV-madgraph WWZNoGstarJets_8TeV-madgraph WWWJets_8TeV-madgraph TTWJets_8TeV-madgraph TTZJets_8TeV-madgraph_v2 TTWWJets_8TeV-madgraph TTGJets_8TeV-madgraph
Signal SMS	SMS-T2tt_FineBin_Mstop-225to1200_mLSP-0to1000_8TeV-Pythia6Z SMS-T2tt_2J_mStop-500_mLSP-300_TuneZ2star_8TeV-madgraph-tauola SMS-T2tt_2J_mStop-750_mLSP-25_TuneZ2star_8TeV-madgraph-tauola SMS-T2tt_2J_mStop-600_mLSP-50_TuneZ2star_8TeV-madgraph-tauola SMS-T2tt_2J_mStop-400_mLSP-150_TuneZ2star_8TeV-madgraph-tauola SMS-T2tt_2J_mStop-250_mLSP-50_TuneZ2star_8TeV-madgraph-tauola SMS-T2tt_mStop-825to900_mLSP-1_and_mLSP-25to800_8TeV-Pythia6Zstar SMS-T2bw_2J_mStop-500to800_mLSP-0to700_x-025_TuneZ2star_8TeV-madgraph-tauola SMS-T2bw_2J_mStop-500to800_mLSP-0to700_x-050_TuneZ2star_8TeV-madgraph-tauola SMS-T2bw_2J_mStop-100to475_mLSP-0to375_x-050_TuneZ2star_8TeV-madgraph-tauola SMS-T2bw_2J_mStop-100to475_mLSP-0to375_x-075_TuneZ2star_8TeV-madgraph-tauola SMS-T2bw_2J_mStop-500to800_mLSP-0to700_x-075_TuneZ2star_8TeV-madgraph-tauola SMS-T2bw_2J_mStop-100to475_mLSP-0to375_x-025_TuneZ2star_8TeV-madgraph-tauola SMS-T2tt_2J_mStop-225to350_mLSP-25to250_LeptonFilter_TuneZ2star_8TeV-madgraph-tauola SMS-T2tt_2J_mStop-100to200_mLSP-1to100_LeptonFilter_TuneZ2star_8TeV-madgraph-tauola
QCD	QCD_Pt_20_30_EMEnriched_TuneZ2star_8TeV_pythia6 QCD_Pt_30_80_EMEnriched_TuneZ2star_8TeV_pythia6 QCD_Pt_80_170_EMEnriched_TuneZ2star_8TeV_pythia6 QCD_Pt_20_MuEnrichedPt_15_TuneZ2star_8TeV_pythia6 QCD_Pt_20_30_BCtoE_TuneZ2star_8TeV_pythia6 QCD_Pt_30_80_BCtoE_TuneZ2star_8TeV_pythia6 QCD_Pt_80_170_BCtoE_TuneZ2star_8TeV_pythia6

Table 1: Signal and background simulated datasets.

The analysis strategy described in the note uses this property of M_{T2} to define a signal region, $M_{T2} > M_W$, which should have a reduced contamination from dileptonic top decays. We estimate the residual contamination of the signal region with SM $t\bar{t}$ and WW events by normalizing simulated backgrounds in a data-driven way using several different control regions. Finally, we perform a counting experiment in the signal region and interpret the results in terms of several different simplified models (SMS) relevant for third generation or natural supersymmetry.

Period	Dataset path
2012A	`/DoubleElectron/Run2012A-22Jan2013-v1/AOD`
	`/DoubleMu/Run2012A-22Jan2013-v1/AOD`
	`/MuEG/Run2012A-22Jan2013-v1/AOD`
2012B	`/DoubleElectron/Run2012B-22Jan2013-v1/AOD`
	`/DoubleMuParked/Run2012B-22Jan2013-v1/AOD`
	`/MuEG/Run2012B-22Jan2013-v1/AOD`
2012C	`/DoubleElectron/Run2012C-22Jan2013-v1/AOD`
	`/DoubleMuParked/Run2012C-22Jan2013-v1/AOD`
	`/MuEG/Run2012C-22Jan2013-v1/AOD`
2012D	`/DoubleElectron/Run2012D-22Jan2013-v1/AOD`
	`/DoubleMuParked/Run2012D-22Jan2013-v1/AOD`
	`/MuEG/Run2012D-22Jan2013-v1/AOD`

Table 2: 8 TeV dilepton triggered datasets.

Channel	HLT path
ee	`HLT_Ele17_CaloIdT_CaloIsoVL_TrkIdVL_TrkIsoVL_Ele8_CaloIdT_CaloIsoVL_TrkIdVL_TrkIsoVL*`
$e\mu$	`HLT_Mu17_Ele8_CaloIdT_CaloIsoVL_TrkIdVL_TrkIsoVL_v*`
	`HLT_Mu8_Ele17_CaloIdT_CaloIsoVL_TrkIdVL_TrkIsoVL_v*`
$\mu\mu$	`HLT_Mu17_(Tk)Mu8_v*`

Table 3: HLT paths used to select events.

2 Selection

2.1 Datasets and trigger selection

The simulated datasets used in this analysis are shown in Table 1. The dilepton triggered data used are shown in Table 2. The HLT paths used to select events in data are shown in Table 3.

2.2 Object selection

The electron object selection is shown in Table 4. Electron candidates are required to have at least 20 GeV (10 GeV) of transverse momentum for the leading (lagging) candidate and fall within $-2.5 < \eta < 2.5$. We veto electrons falling into the EB-EE overlap region. We apply the standard veto on conversion electrons. The VBTF WP80 selection is used to identify good quality electron candidates consistent with the primary vertex position. Finally, we require that the isolation sum relative to the p_T of the electron be less than 0.15 to ensure that the electron is well isolated. We use reco::Electron objects but the isolation sum comes from the corresponding PF object.

The muon object selection is shown in Table 5. Muon candidates are required to have at least

Cut	Value
Type	reco::Electron
p_T	> 20 GeV (leading)
p_T	> 10 GeV (lagging)
$\|\eta\|$	< 2.5
	veto EB/EE overlap region
conversion veto	applied
ID working point	VBTF WP80
relIso (ρ corrected)	< 0.15

Table 4: Electron object selection.

Cut	Value
Type	reco::Muon
ID	GlobalMuonPromptTight
p_T	> 20 GeV (leading)
p_T	> 10 GeV (lagging)
$\|\eta\|$	< 2.4
d_0	< 0.2 cm
d_z	< 0.5 cm
relIso($\delta(R) < 0.3$)	< 0.15

Table 5: Muon object selection.

Cut	Value
algorithm	AK5PFchs
p_T	30 GeV
$\|\eta\|$	< 2.4
jet ID	loose PFJetID
b-tag	CSV medium

Table 6: Jet object selection

20 GeV (10 GeV) of transverse momentum for the leading (lagging) candidate and fall within $-2.4 < \eta < 2.4$. We require that they be PFMuons that pass the GlobalMuonPromptTight identification. We require the transverse (longitudinal) impact parameter with respect to the primary vertex to be less than 2 (5) mm. Finally, we require that the isolation sum relative to the p_T of the electron be less than 0.15 to ensure that the muons are well isolated. We use reco::Muon objects but the isolation sum comes from the corresponding PF candidate.

The jet object selection is shown in Table 6. Jet candidates are required to have at least 30 GeV of transverse momentum and fall within $-2.4 < \eta < 2.4$. Jet are required to pass the loose PFJetID, which selects only jets with EM and hadronic energy fractions consistent with a real jet. In order to consider a jet as b-tagged we also require that the jet pass the medium working point of the combined secondary vertex (CSV) tagging algorithm.

2.3 Event selection

Using the object definitions from Section 2.2, we proceed to define an event selection shown in Table 7. We require at least two oppositely charged e and/or μ with an invariant mass larger that 20 GeV. Same-flavor lepton pairs are vetoed if the invariant mass of the leptons is within 25 GeV of the Z mass. In the case where both leptons have the same flavor (SF), we additionally ask for at least 40 GeV of $E_{\mathrm{T}}^{\mathrm{miss}}$ in order to suppress the SM background from Drell-Yan pairs

Object	Selection
e, μ	At least two, oppositely charged
	Highest sum-p_T pair used
M_{ee} or $M_{\mu\mu}$	$M < 76 \cup M > 106$
$E_{\mathrm{T}}^{\mathrm{miss}}$	> 40 in $ee, \mu\mu$ channels
$M_{\ell\ell}$	> 20 GeV (all flavors)
N_{jets}	≥ 2
N_b	≥ 1

Table 7: Event selection

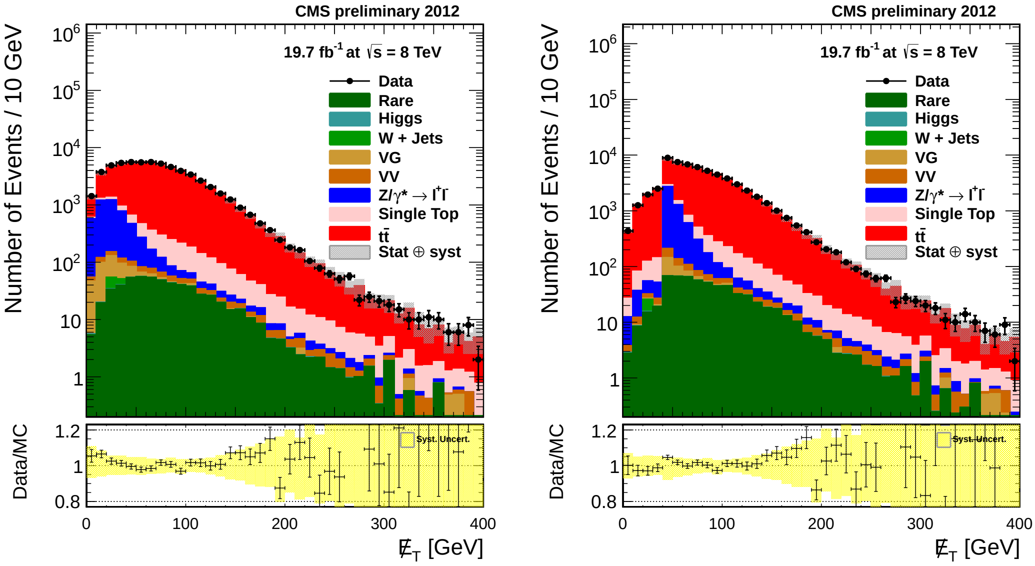

Figure 1: Selected events before (left) and after (right) the E_T^{miss} cut on same flavor events. The Drell-Yan contribution is efficiently removed by the E_T^{miss} requirement.

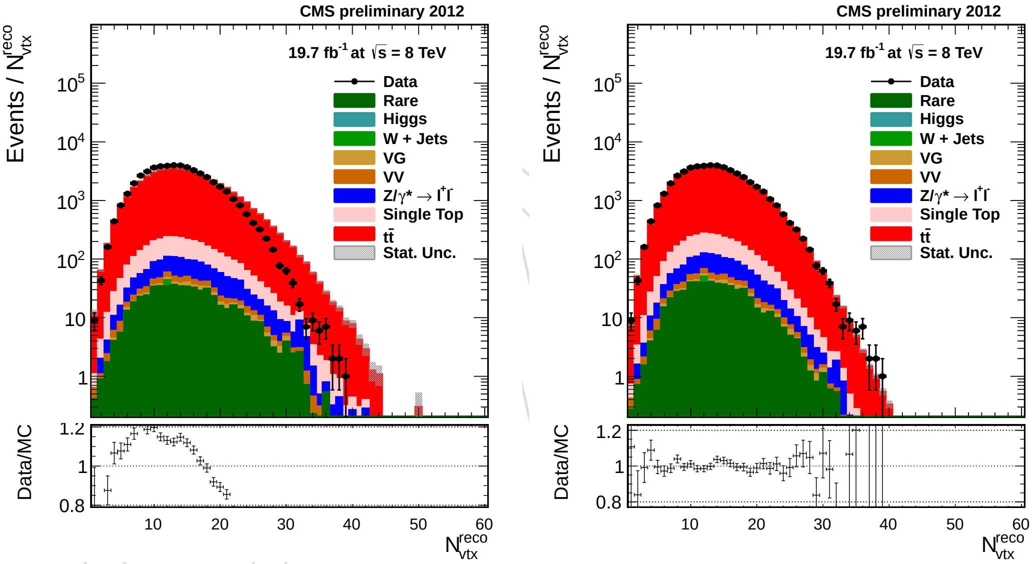

Figure 2: Number of reconstructed vertices in simulation and data, before reweighting (left) and after (right). Statistical uncertainty on simulation is indicated by the gray shaded band; on data, by black error bars. NB that signal and background Monte Carlo require different reweighting schemes.

which pass the invariant mass requirement. The effect of this requirement can be seen in Figure 1. To further suppress this and other vector boson backgrounds, we require at least two jets and one of them must be b-tagged.

2.4 Pile-up reweighting

The number of pile-up interactions per event affects the analysis in several ways. Pile-up reduces the probability of identifying the correct primary vertex in the event. It worsens the energy resolution for the selected objects (especially jets and E_T^{miss}), and makes lepton identification more difficult by putting additional energy into the isolation cones of lepton candidates.

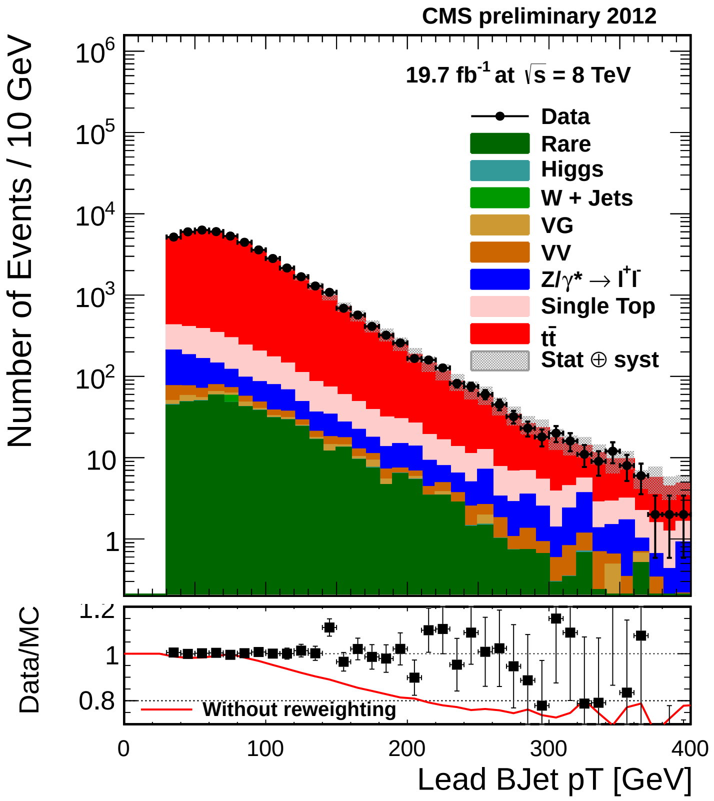

Figure 3: b-jet p_T spectrum after top p_T reweighting. The effect of the reweighting can be seen in the ratio plot at bottom. The reweighting decreases the number of high-p_T tops in simulation. Without reweighting (red line) we would observe an excess of high b-jet p_T events in the simulation with respect to the data.

It has similar effects at the trigger level. For all these reasons, we reweight the simulation events to have the same pile-up distribution as in data. Since the LHC ran at 50 ns bunch spacing in 2012, we are primarily concerned with the effect of in-time pileup. As a result, we determine the event weights using the Poisson mean for the true number of pileup vertices in the event. Figure 2 displays the number of reconstructed primary vertices in data and simulation, before and after the pile-up weights are applied. We apply the full object and event selection for this plot. The reweighting procedure results in good agreement between the distribution of number of vertices in the simulation with our selected data sample.

2.5 Top p_T reweighting

The Top PAG recommends reweighting the $t\bar{t}$ p_T spectrum according to the following formula:

$$w(p_T) = e^{0.156-0.00137 p_T} \tag{4}$$

where p_T is the geometric average of the t and $\bar{t}$ p_T for a given event.[1] The overall effect of this reweighting is to decrease the number of top pair events with large p_T. It improves agreement between data and simulation for large values of top decay product p_T as can be seen in the E_T^{miss} distribution in Figure 3.

---

[1] https://twiki.cern.ch/twiki/bin/viewauth/CMS/TopPtReweighting

3 Backgrounds

The object selection described in Section 2 rejects most standard model backgrounds; only final states which contain two high-p_{T} lepton candidates along with two jets with one b-tag contribute to the background. The dominant sources of background and their approximate contributions to the selected sample for $M_{T2} > 80$ GeV are the following:

- $t\bar{t}$: 90%
- Drell-Yan: 4%
- tW: 4%
- diboson: <1%
- other (fake leptons): 1%

We evaluate the contributions of the Drell-Yan and fake lepton backgrounds in a data-driven way using control samples. The rate of the EW backgrounds is taken from simulation. The remainder is considered as $t\bar{t}$ and normalized to the control region with $MT_2 < 80$ GeV.

3.1 Description of the "$R_{out/in}$ method"

The analysis makes use of a data-driven Drell-Yan estimation method described in reference [?]. For the same-flavor we use the DY MC listed in Tab. 1 and we extract the so-called $R_{out/in}$ parameter, that is defined as the ratio of the events outside the Z-veto, as defined in 2.2, divided by the events falling inside that region:

$$R_{out/in} = \frac{N^{out}_{DYMC}}{N^{in}_{DYMC}} \tag{5}$$

This ratio is then applied to the number of data events falling inside the Z-veto region ($N^{l^+l^-}_{in}$) to predict the number of expected events in data ouside the Z-veto region. $N^{l^+l^-}_{in}$ can be contaminated by non-DY processes, such as $t\bar{t}$, therefore we subtract from $N^{l^+l^-}_{in}$ the number of events with opposite-flavour ($N^{e\mu}_{in}$). Since electrons and muons may have different reconstruction effieincies we use the k factors defined in Eq. 6 to account for these.

$$k_{ee} = \sqrt{\frac{N^{e^+e^-}_{in}}{N^{\mu^+\mu^-}_{in}}} \quad k_{\mu\mu} = \sqrt{\frac{N^{\mu^+\mu^-}_{in}}{N^{e^+e^-}_{in}}} \tag{6}$$

Hence the number of events outside the Z-veto window can be measured from data as:

$$N^{l^+l^-,obs}_{out} = R^{l^+l^-}_{out/in}(N^{l^+l^-}_{in} - 0.5N^{e\mu}_{in}k_{ll}) \tag{7}$$

where the factor 0.5 is used to account for combinatorics of the $e\mu$ sample.

3.1.1 Results using MC based $R_{out/in}$

The results obtained using this method are summarized in Tab. 8, the results are shown divided for the two same-flavor channels and for different stages of the selection. The differences between simulation and data driven estimates are coming from the discrepancies already observed in the $E_{\mathrm{T}}^{\mathrm{miss}}$ and jet distributions between data and MC.

	$\geq$ 2 jets	$\geq$ 2 jets + $E_{\mathrm{T}}^{\mathrm{miss}}$	$\geq$ 2 jets + $E_{\mathrm{T}}^{\mathrm{miss}}$ + b-tag
ee			
DY MC	14877.4 ± 53.0	2154.7 ± 18.0	236.13 ± 6.08
DY data-driven estimate	15613.0 ± 75.4	2626.2 ± 32.6	331.56 ± 14.54
$R_{out/in}$	0.1417 ± 0.0005	0.1644 ± 0.0015	0.1668 ± 0.0045
SF data/MC	1.0494 ± 0.0063	1.2188 ± 0.0183	1.4041 ± 0.0714
$\mu\mu$			
DY MC	27049.9 ± 73.6	4155.2 ± 25.2	415.00 ± 7.84
DY data-driven estimate	30217.7 ± 113.7	5361.6 ± 51.6	663.51 ± 22.68
$R_{out/in}$	0.1729 ± 0.0005	0.2144 ± 0.0014	0.2011 ± 0.0041
SF data/MC	1.1171 ± 0.0052	1.2904 ± 0.0147	1.5988 ± 0.0624
$e\mu$			
DY MC	2224.1 ± 16.5	2224.1 ± 16.5	208.65 ± 4.90
DY data-driven estimate	2408.0 ± 20.1	2408.0 ± 20.1	312.62 ± 12.42
SF data/MC	1.0827 ± 0.0041	1.0827 ± 0.0041	1.4983 ± 0.0480

Table 8: Data-driven Drell-Yan background estimation in the *ee* and $\mu\mu$ channels compared with simulation, for several steps of the analysis.

3.1.2 Prediction in the opposite-flavor channel

The previous method can be simply applied in the $e\mu$ channel using the mean of the two scale factors, i.e. $SF_{e\mu} = \sqrt{SF_{ee} \times SF_{\mu\mu}}$, obtained for the *ee* and $\mu\mu$ channels.

As cross check we have also used another technique, we fit the various MC components to data in order to extract the proper Drell-Yan scale factor. We use all the available MC for the fit, of which of course the $t\bar{t}$ is the larger component, to determine the relative amount of the DY part with respect to the MC. The coefficients of the fit and their errors will determine the scale factors applied in the $e\mu$ channel, these are listed in Tab. 9.

	$\geq$ 2 jets	$\geq$ 2 jets + $E_{\mathrm{T}}^{\mathrm{miss}}$	$\geq$ 2 jets + $E_{\mathrm{T}}^{\mathrm{miss}}$ + b-tag
$e\mu$			
DY MC	2224.1 ± 16.5	2224.1 ± 16.5	208.65 ± 4.90
DY data-driven estimate	2317.9 ± 164.5	2317.9 ± 164.5	412.32 ± 137.01
SF data/MC	1.0422 ± 0.0746	1.0422 ± 0.0746	1.9761 ± 0.6584

Table 9: Data-driven Drell-Yan background estimation in the $e\mu$ channels compared with simulation, for several steps of the analysis.

3.2 Fake lepton estimation

Semileptonic top pair events and leptonically decaying W plus jets events can pass the signal selection if one of the jets in the event is misreconstructed as an isolated lepton. To guard against the possibility that the jet to lepton fake rate is not well modelled in the simulation, we perform a data-driven estimate of this probability using the so-called "tight-to-loose" method. As its name suggests, it relies on defining two working points for the muon and electron identification and isolation requirements: a tight one, which is the one used in the analysis, and a loose one, which defines the *"fakeable object"* and differs from the tight one because of relaxed lepton isolation cuts.

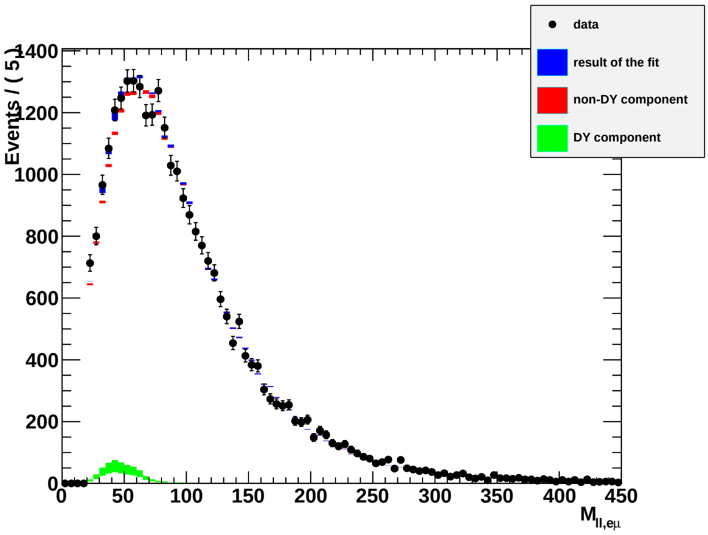

Figure 4: Result of the fits used to estimate the $e\mu$ background at th last step of the selection. In green is the DY component while in red the non-DY, the result of the fit (blue) and the data points are well in agreement.

The method is described in [?] and in [?] and used e.g. in [?]. It consists of two steps. In the first one, fake and prompt rates are measured from data, in a phase space region enriched with QCD dijet events and $Z \rightarrow \ell\ell$ events, respectively. Both quantities are defined as the fraction of fakeable objects that also pass the tight selection. These ratios are parametrized as a function of p_T and η of the fakeable object.

In the second step, data events are required to pass the loose lepton requirements and the signal selection cuts. From this set of loose-loose dilepton events, the W+jets event yield can be extracted by means of some formulae combining fake and prompt rate.

The muon and electron prompt rates are obtained with a standard tag-and-probe technique applied on data. Results are shown in Table 10.

Table 10: Measured electron and muon prompt rates in bins of p_T and η of the fakeable object. Uncertainties are statistical only.

electron prompt rate		
p_T (GeV)	$0 < \eta \leq 1.4442$	$1.566 < \eta \leq 2.5$
$10 < p_T \leq 15$	0.833 ± 0.015	0.75 ± 0.02
$15 < p_T \leq 20$	0.872 ± 0.007	0.785 ± 0.013
$20 < p_T \leq 25$	0.902 ± 0.004	0.828 ± 0.008
$25 < p_T \leq 50$	0.9592 ± 0.0005	0.904 ± 0.001
$50 < p_T$	0.9783 ± 0.0010	0.942 ± 0.003

muon prompt rate		
p_T (GeV)	$0 < \eta \leq 1.479$	$1.479 < \eta \leq 2.4$
$10 < p_T \leq 15$	0.837 ± 0.009	0.844 ± 0.009
$15 < p_T \leq 20$	0.881 ± 0.005	0.895 ± 0.005
$20 < p_T \leq 25$	0.915 ± 0.003	0.935 ± 0.003
$25 < p_T \leq 50$	0.9754 ± 0.0003	0.9761 ± 0.0005
$50 < p_T$	0.9918 ± 0.0005	0.9921 ± 0.0008

The muon and electron fake rates are extracted from a phase space dominated by QCD dijet events, which are selected by using the single lepton trigger paths listed in Table 11. The cuts defining this control region aim at reducing the contribution from W or Z leptonic decays. Events with W decays are rejected by requiring PF $E_T^{miss} < 20$ GeV and, only for the muon fake rate, that the W candidate transverse mass be less than 15 GeV. Events with Z decays are discarded by vetoing the Z mass window: $m_{\mu\mu} \notin [76, 106]$ GeV, $m_{ee} \notin [60, 120]$ GeV. Events with low-mass dilepton resonances are removed by the additional $m_{\ell\ell} > 20$ GeV requirement.

The bias introduced by electroweak contaminations from leptons in W+jets and Z+jets events is removed in two ways. The tight (loose) lepton yields obtained from W+jets and Z+jets simulated samples are subtracted from data in the numerator (denominator) of the fake rate definition. Moreover, the residual bias for high p_T^ℓ values is avoided by assuming that lepton fake rate flattens out for $p_T^\ell > 35$ GeV.

An additional threshold is introduced on the p_T of a so-called *"away-side"* jet. It is a jet that is separated by at least $\Delta R(j_{away}, \ell) > 1.0$ from a loose lepton, which is required to be within a distance $\Delta R(j_{away}, \ell) < 0.3$ from a so-called *"near-side"* jet. This jet p_T requirement is motivated by the fact that the energy spectrum of jets misidentified as leptons can be different from the one of real jets. The relative isolation of a loose lepton is a sensitive variable to these differences in jet energy. Hence, by cutting on the away-side jet p_T (not on the near-side one, to avoid biases), the di-jet control sample from which the fake rate is extracted can be made more similar to the non-prompt background component contributing to the final event yield.

The lepton yields, extrapolated from the loose-loose to the tight-tight same-sign dilepton region, obtained with different requirements on the away-side jet p_T and on the loose lepton isolation, are compared with the ones extracted from data events containing a tight-tight same-sign lepton pair, with one lepton passing the quality criteria used in the analysis, the other one a looser selection. Contaminations from processes different from semileptonic or all-hadronic $t\bar{t}$ and from W+jets have been estimated from simulation and subtracted from this control sample. The threshold on jet p_T is then chosen as the one giving the best agreement.

The results can be found in Fig. 5 for muons and electrons. In the muon case the best jet p_T threshold turns out to be around 50 GeV without any isolation requirement on loose muons.

Table 11: Single lepton trigger paths used in the enriched QCD sample event selection.

Electron triggers HLT_Ele17_CaloIdT_CaloIsoVL_TrkIdVL_TrkIsoVL_v*	HLT_Ele8_CaloIdT_CaloIsoVL_TrkIdVL_TrkIsoVL_v
Muon triggers	HLT_Mu8_v* HLT_Mu17_v*

The results obtained for the electron and muon fake rate are listed in table 12 for muons and electrons.

To extract the non-W/Z lepton event yield, the event selection is applied to data, but requiring that both leptons pass the loose lepton quality cuts.

Let $\varepsilon = \frac{f}{1-f}$ and $\eta = \frac{1-p}{p}$. Events are classified according to the number of leptons passing or failing the tight requirements. The weights assigned to each events are:

$$\mathrm{Pass-Pass:}\ w_{P_1P_2} = -\frac{\varepsilon_1\eta_1 + \varepsilon_2\eta_2 - \varepsilon_1\varepsilon_2\eta_1\eta_2}{(1-\varepsilon_1\eta_1)(1-\varepsilon_2\eta_2)} \tag{8}$$

$$\mathrm{Fail-Fail:}\quad w_{F_1F_2} = -\frac{\varepsilon_1\varepsilon_2}{(1-\varepsilon_1\eta_1)(1-\varepsilon_2\eta_2)} \tag{9}$$

$$\mathrm{Pass-Fail:}\quad w_{P_1F_2} = \frac{\varepsilon_2}{(1-\varepsilon_1\eta_1)(1-\varepsilon_2\eta_2)} \tag{10}$$

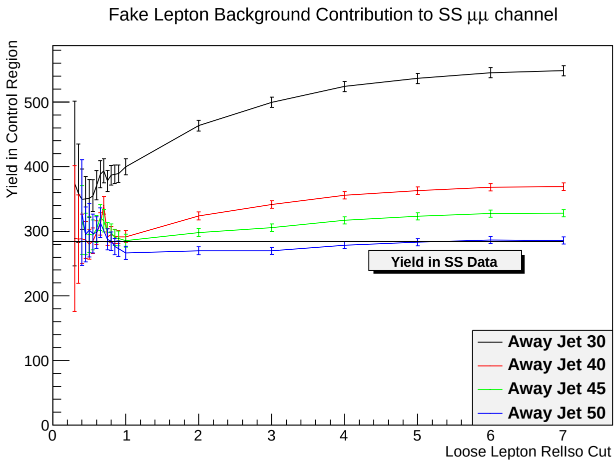

Figure 5: Comparison between lepton yields in the tight-tight same-sign dilepton region as a function of the corresponding threshold on the loose lepton relative isolation, for muons in the $\mu\mu$ channel. The colored lines refer to different jet p_T thresholds used to select events in the di-jet control sample. The black horizontal line refers to data minus backgrounds different from semileptonic or all-hadronic $t\bar{t}$ and W+jets, as obtained from a tight-tight same-sign dilepton sample enriched with W+jets events.

Table 12: Measured electron and muon fake rates in bins of p_T and η of the fakeable object. Uncertainties are statistical only.

electron fake rate				
p_T (GeV)	$0 < \eta \leq 1.0$	$1.0 < \eta \leq 1.479$	$1.479 < \eta \leq 2.0$	$2.0 < \eta \leq 2.5$
$10 < p_T \leq 15$	0.51 ± 0.02	0.46 ± 0.03	0.46 ± 0.03	0.40 ± 0.03
$15 < p_T \leq 20$	0.36 ± 0.03	0.33 ± 0.04	0.34 ± 0.04	0.34 ± 0.04
$20 < p_T \leq 25$	0.36 ± 0.03	0.32 ± 0.03	0.32 ± 0.03	0.33 ± 0.03
$25 < p_T \leq 30$	0.38 ± 0.04	0.23 ± 0.04	0.29 ± 0.04	0.30 ± 0.03
$30 < p_T \leq 35$	0.28 ± 0.04	0.26 ± 0.06	0.23 ± 0.04	0.24 ± 0.05

muon fake rate				
p_T (GeV)	$0 < \eta \leq 1.0$	$1.0 < \eta \leq 1.479$	$1.479 < \eta \leq 2.0$	$2.0 < \eta \leq 2.4$
$10 < p_T \leq 15$	0.31 ± 0.03	0.32 ± 0.04	0.38 ± 0.05	0.44 ± 0.08
$15 < p_T \leq 20$	0.16 ± 0.03	0.17 ± 0.05	0.21 ± 0.06	0.19 ± 0.10
$20 < p_T \leq 25$	0.161 ± 0.016	0.17 ± 0.03	0.21 ± 0.03	0.30 ± 0.06
$25 < p_T \leq 30$	0.103 ± 0.019	0.24 ± 0.04	0.16 ± 0.04	0.38 ± 0.11
$30 < p_T \leq 35$	0.101 ± 0.024	0.10 ± 0.04	0.17 ± 0.05	0.15 ± 0.11

$$\text{Fail} - \text{Pass} : \quad w_{P_2F_1} = \frac{\varepsilon_1}{(1-\varepsilon_1\eta_1)(1-\varepsilon_2\eta_2)} \tag{11}$$

The total yield of non-W/Z lepton events is then given by the sum of all the event weights in each final state. The two terms in Eqs. 8 and 9 give a negative contribution to the total event yield.

Results are shown in Table 3.2 together with the statistical and systematical uncertainties. The former ones have been calculated by varying both the muon and the electron fake rates in each bin up- and downwards by their statistical uncertainty and by taking the largest difference between the resulting yields and the central value. The latter ones have been evaluated in a similar way, but by varying the threshold used in the leading jet E_T cut by ±5 GeV for muons and by ±10 GeV for electrons.

after $N_{b-tags} \geq 1$				
channel	central value	stat.	syst.	stat. $\oplus$ syst.
$\mu\mu$	642	±18%	±4%	±18%
ee	97	±27%	±15%	±31%
$e\mu$	643	±28%	±6%	±29%

after $M_{T2}(\ell\ell) > 110$ GeV				
channel	central value	stat.	syst.	stat. $\oplus$ syst.
$\mu\mu$	1.09	±37%	±15%	±40%
ee	0.89	±24%	±18%	±30%
$e\mu$	0.91	±32%	±12%	±34%

3.3 $t\bar{t}$ estimation

After determining the contribution to the control region $M_{T2} < 80$ GeV from Z events and fake leptons by the previously described methods, and of the rare backgrounds from simulation, we estimate the normalization of the remaining top pair background by subtracting these estimates from the number of data events with $M_{T2} < 80$ GeV in both data and simulation and then scaling the number of $t\bar{t}$ events in the simulation to match the data. We obtain a scale

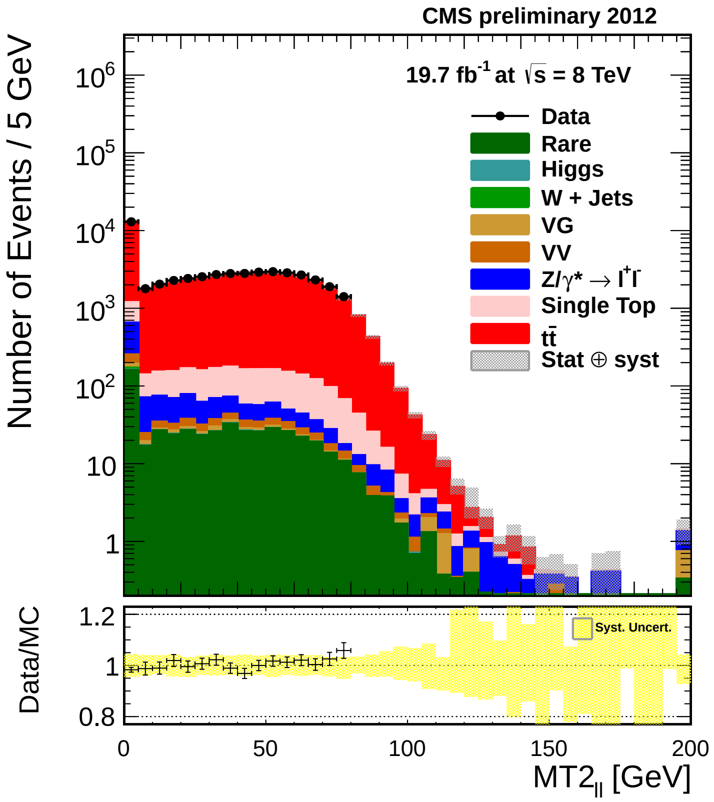

Figure 6: $M_{T2}(ll)$ distribution, used to obtain the normalization and normalization uncertainty for $t\bar{t}$ events.

factor of 1.007 with negligible statistical uncertainty. The normalization to the control region is displayed in Figure 6 for events passing the full object and event selection.

Signal contamination in the normalization region is handled using the Monte Carlo prediction. The fraction of signal misidentified as tt when performing this procedure is tracked for each signal point, and the overprediction of the background is accounted for in the limit-setting procedure. In general the effect is vanishingly small except at low mass when the splitting between the top and LSP mass is equal to the top mass, when the signal contamination can be as high as 10% and the shapes are similar for signal and background. Otherwise, the effect is typically of order one per mille.

One feature of Figure 6 which is not directly related to the background normalization yet bears some discussion is the peak in the M_{T2} distribution near zero. Since the computation of M_{T2} involves finding the minimum possible value for each event, solutions with $M_{T2} = 0$ will be kept if found. An example of an event for which $M_{T2} = 0$ would be one with back-to-back leptons, where the $E_{\mathrm{T}}^{\mathrm{miss}}$ vector points along one of the lepton vectors. In this case, any partition of the $E_{\mathrm{T}}^{\mathrm{miss}}$ vector along the lepton-lepton line will result in identically zero M_T for each side of the system and a total M_{T2} of zero. Other configurations can also have an M_{T2} of zero so long as a solution with zero transverse mass along each lepton can be found.

3.4 Summary

Estimated background yields and their associated uncertainties for $M_{T2} > 110$ GeV are displayed in Table 13. The mean background expectation for three different M_{T2} cuts are displayed in Table 14.

Bkg.	Events	Stat. unc.	Sys. unc.
$t\bar{t}$	15.2	1.6	+4.3 -1.5
DY + jet(s)	5.9	0.8	+2.9 -1.5
$V\gamma$	1.8	0.8	+3.2 -0.9
single t	2.0	0.1	+0.2 -0.2
VV	0.6	0.2	+0.2 -0.3
other (e.g. W, H)	2.7	0.2	+0.6 -0.5

Table 13: Background prediction in the signal region $M_{T2} > 110$ GeV with statistical (MC statistics) and systematic uncertainties.

M_{T2} value	Expected bkg.	Stat. unc.	Sys. unc.	
80	1702.4	17.2	+110.6	-113.1
90	414.0	8.2	+44.0	-38.8
100	101.5	3.9	+11.5	-12.7
110	28.2	2.0	+7.1	-2.4
120	12.9	1.2	+3.4	-1.4

Table 14: Background expectation for five different M_{T2} cut values.

4 Systematic uncertainties

The sensitivity of this analysis is affected both by uncertainties on the background contribution in the signal region as well as on the acceptance and efficiency for the signal models considered. Here we present studies of the size of the dominant systematic uncertainties.

4.1 Trigger efficiencies

The method uses events selected by a trigger selection weakly correlated with dilepton triggers (cross triggers) and counts the number of such events passing and failing the dilepton trigger selection. More details can be found in AN-12-389. The MET based datasets were selected as the cross triggers, as they were found to be weakly correlated with dilepton triggers and to have a large enough number of events to keep the statistical uncertainty below 1%. The measured efficiencies were compared to the efficiencies in MC for $t\bar{t}$ events (TTJets Madgraph sample, full sim) and the signal sample (fast sim reconstruction). In both cases the corresponding pileup corrections were applied.

In order to keep the statistical uncertainty as small as possible a set of 50 MET trigger bits was

Source	Uncertainty
ϵ(trigger)	1.2%
$\epsilon(\ell)$	1.8%
ℓ energy scale	1.7%
ϵ(b-tag)	5.0%
gen top p_{T}	0.5%
JES	13.5%
JER	9.3%
unclustered energy	7.3%
Total	19.1%

Table 15: Systematic uncertainties on the background yield in the signal region $M_{T2} > 110$ GeV by source. In cases where the error is asymmetric the larger of the two errors is displayed. The full asymmetric error is used in the limit calculation.

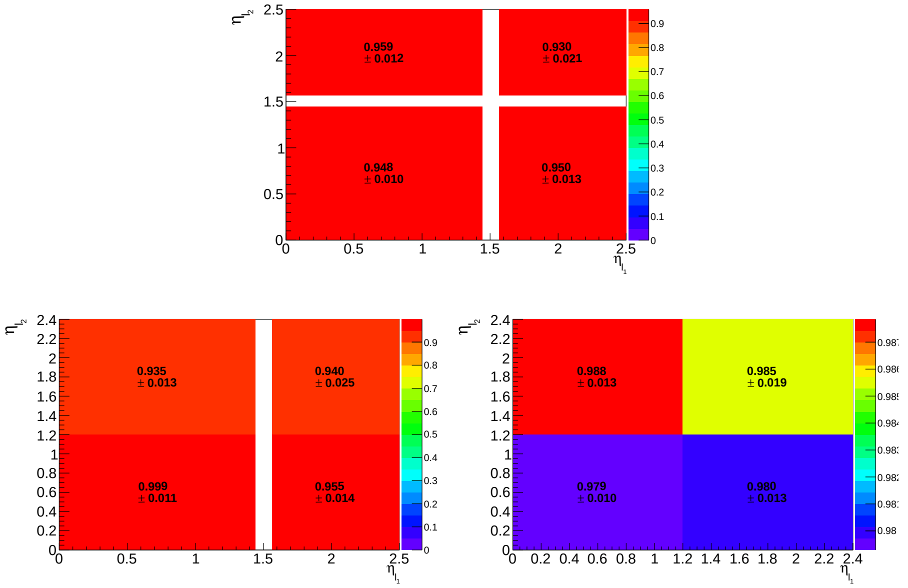

Figure 7: Trigger scale factors as a function of (η_{l_1}, η_{l_2}) for the ee (top), $e\mu$ (bottom left), and $\mu\mu$ (bottom right) trigger. (**ttbar sample**)

selected for the efficiency estimation. The total systematic uncertainty on the measured trigger dilepton efficiencies is conservatively estimated to be 1%, to account not only for the correlation but also for other factors, for instance the possible difference between the behaviour of triggers in data and simulationi, or for a bias intrinsic to the selected MET dataset.

The dilepton trigger efficiency measured in data and MC and the resulting global scale factors applied to correct the simulation yield are summarized in Table 16 and Table 17.

The scale factors are stable within the uncertainties with respect to the lepton transverse momentum. In order to take into account the small dependence on the lepton pseudorapidity, the scale factors are determined double-differentially in η. Figures 7, 8 show these scale factors for the dielectron, dimuon, and $e\mu$ channel used to correct the background (full sim) and signal (fast sim) yields.

4.2 Lepton identification and isolation efficiencies

Lepton efficiencies are estimated using a tag and probe method, following a simple cut and count based approach (except for the lowest p_{T} bin, where a fit is used to account for the non negligible background contribution). In order to estimate the efficiency such that the measurement is uncorrelated from the dilepton trigger efficiency, single lepton triggered data samples are used. Dilepton candidates compatible with the Z mass are assumed to come from the Z bosons and used to estimate the efficiency. The tag and probe leptons are matched requiring opposite charge and an invariant mass in the range $76 < \mathrm{m}_{ll} < 106$ GeV. The definition of ”tag” leptons corresponds to the complete isolation and identification used in the analysis. Tag leptons in both channels are selected if they are associated to an HLT lepton. The trigger bits selected are HLT_IsoMu24_eta2p1 and HLT_IsoMu24 for the single muon dataset and HLT_Ele27_WP80 for the single electron.

The measured efficiencies are compared to the results in MC Drell-Yan (FullSim and FastSim), where the pileup correction is applied to extract the scale factors ($SF_l = \epsilon_l^{data}/\epsilon_l^{MC}$) used to

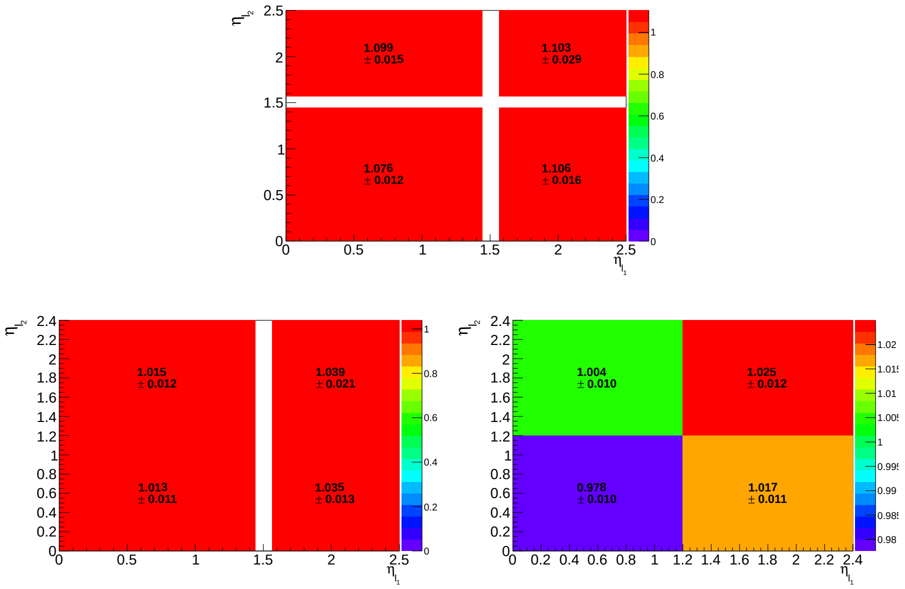

Figure 8: Trigger scale factors as a function of (η_{l_1}, η_{l_2}) for the ee (top), $e\mu$ (bottom left), and $\mu\mu$ (bottom right) trigger. (**SUSY sample**)

correct the MC predictions. The global identification and isolation efficiencies and scale factors are presented in Table 4.2, both for the full and fast simulation samples.

In order to account for the dependence of the SF on p_T and η of the leptons, 2D scale factors are applied in the analysis. Figure 10 shows the total scale factors as a function of (η, p_T) of the lepton, obtained with fast and full simulation.

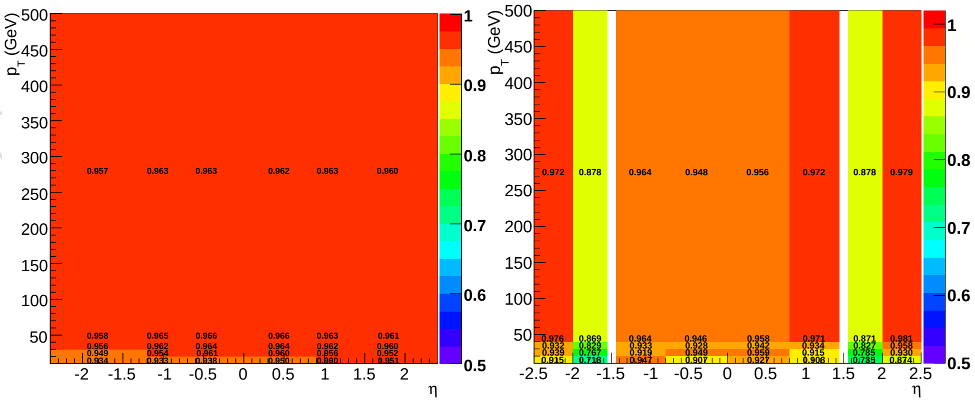

Figure 9: Global SF for the FastSim samples as a function of (η,p_T) of the lepton, for muons (left) and electrons (right).

The systematic uncertainties of the lepton efficiencies are estimated by varying the invariant mass window and the tag lepton selection and reapplying the tag and probe method. The largest variation of the scale factors with respect to their nominal value found is about 0.5%. A total systematic uncertainty of 1% in the scale factor is considered, to account as well for differences between Z and $t\bar{t}$-like event kinematics.

We do not observe any substantial correlation between the value of M_{T2} and the size of the

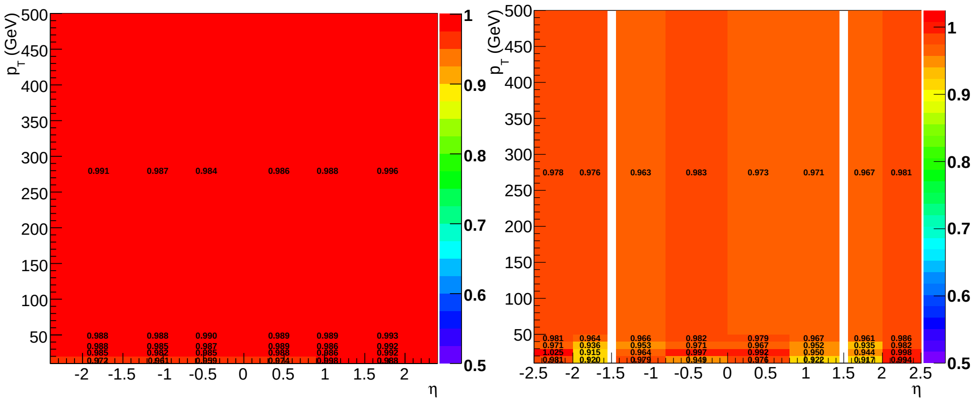

Figure 10: Global SF for the background samples (FullSim) as a function of (η,p$_T$) of the lepton, for muons (left) and electrons (right).

systematic uncertainty.

4.3 b-tag efficiency

We use the b-tag efficiency scale factors and associated uncertainties from AN-12-470. We then vary the scale factor in simulation between $\pm 1\sigma$ from the central value and track the change in the expected background yield in the signal region. NB that separate factors are used for FullSim and FastSim samples.

4.4 Jet Resolution Correction for the measurement of $E_{\mathrm{T}}^{\mathrm{miss}}$

The simulation doesn't model the energy resolution of jets with full accuracy. This subsequently affects the modeling of $E_{\mathrm{T}}^{\mathrm{miss}}$ in the simulation. The JME group has provided a tool that smears the energy of jets in the simulation according to the official JER prescription and subsequently propagates these smeared jets into the $E_{\mathrm{T}}^{\mathrm{miss}}$ calculation. Utilizing a separate set of simulation samples with representative event topologies – $t\bar{t}$, DY + jets, etc. – we calculated the effects of this smearing on the two components of the $E_{\mathrm{T}}^{\mathrm{miss}}$ vector and the dependence of this smearing on the event's unsmeared $E_{\mathrm{T}}^{\mathrm{miss}}$. We then utilized these calculated results as template smearing functions to generate smeared $E_{\mathrm{T}}^{\mathrm{miss}}$ vectors for the $E_{\mathrm{T}}^{\mathrm{miss}}$ in our simulation samples. Due to their small contribution in the signal region we did not apply this process to the rare backgrounds.

The results of this smearing are shown in Figure 11.

4.5 $E_{\mathrm{T}}^{\mathrm{miss}}$ uncertainties propagated to M_{T2}

The $E_{\mathrm{T}}^{\mathrm{miss}}$ measurement is affected by uncertainties on the energy scales and resolutions of all other objects in the event. Of special concern are the uncertainties on jet energy scale, jet energy resolution, and the scale of the unclustered energy in the event. In order to evaluate the effect of these uncertainties we utilized a combination of several prescriptions.

For the lepton and jet energy scales, we varied the objects within systematic uncertainties taken from their respective POGs, propagating the shifted objects back into the $E_{\mathrm{T}}^{\mathrm{miss}}$ calculation. For the leptons, the shifted objects themselves are also used in the calculation of M_{T2}.

For the unclustered energy scale and jet energy resolution uncertainties we utilized the separate

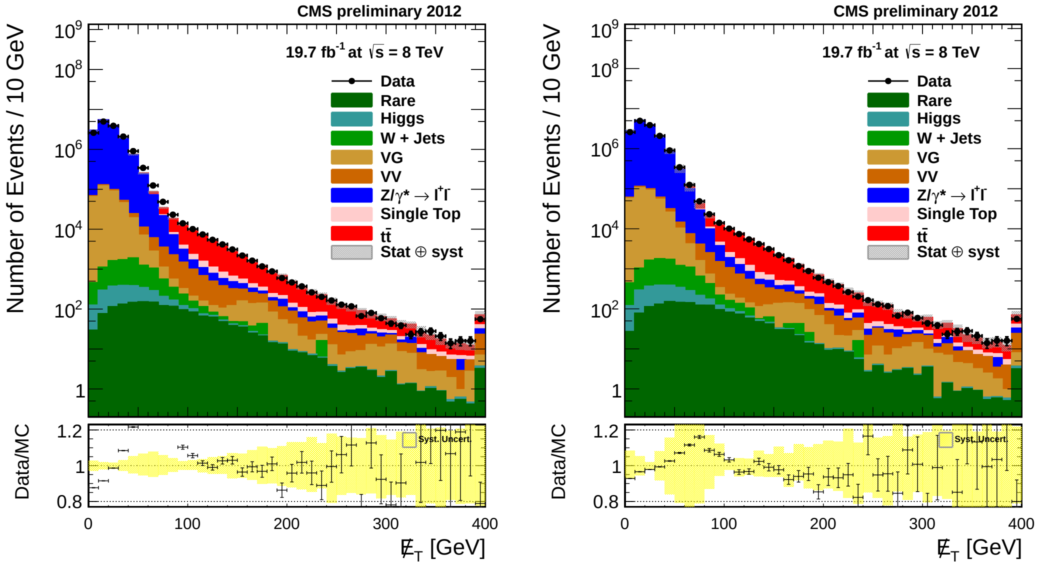

Figure 11: $E_{\mathrm{T}}^{\mathrm{miss}}$ distribution in the inclusive dilepton sample before (left) and after (right) correcting the JER in simulation. Note that the modeling of the DY + jets background below 100 GeV is much better post-smearing.

simulation samples mentioned in Section 4.4. In addition to the information on smeared $E_{\mathrm{T}}^{\mathrm{miss}}$, these samples also contain separate versions of the smeared $E_{\mathrm{T}}^{\mathrm{miss}}$ where the smearing factors (i.e. magnitude of the smearing) for the jets have been varied within $\pm 1\sigma$ of the central value and where the energy scale for unclustered PF candidates has been varied within $\pm 1\sigma$ (10%) of the central value. As with the basic smearing, we calculated template smearing functions with the systematic shifted versions (unclustered energy scale and JER smearing factor) of $E_{\mathrm{T}}^{\mathrm{miss}}$. We propagated all calculated systematic uncertainties on the $E_{\mathrm{T}}^{\mathrm{miss}}$ measurement to the M_{T2} measurement by recalculating M_{T2} for each systematic shift version of the $E_{\mathrm{T}}^{\mathrm{miss}}$ measurement.

4.6 Other systematics

Since the rare electroweak background yields are estimated from simulation, we varied the normalization of these backgrounds in order to check the effects in case the true cross section is far from the prediction. Even with an extreme variation of 50% of the cross section the change in the background yield was at the one percent level since these backgrounds make up only a few percent of the total yield. Since the other uncertainties are much larger we do not use this uncertainty in the final result.

We also considered the effect of variations of the W mass on the background yield. However the current world average uncertainty on the W mass is only 15 MeV and the uncertainty on the width is only 42 MeV. Since these uncertainties are much smaller than the $E_{\mathrm{T}}^{\mathrm{miss}}$ resolution and therefore much smaller than the M_{T2} resolution we do not use this uncertainty in the final result.

The composite effect of all systematic uncertainties is shown in Figure 6.

5 M_{T2} shape analysis

This analysis depends on our understanding of the M_{T2} shape. Consequently, we performed a number of studies with toy simulations and the full simulation to determine how well this shape is understood. We also compared the shape in control regions in data with the prediction of the simulation to check for unanticipated effects.

Since M_{T2} is constructed from $E_{\mathrm{T}}^{\mathrm{miss}}$ and two leptons, the tail at high values can come from a number of different factors:

1. Resolution for lepton p_{T} or direction.
2. Resolution for $E_{\mathrm{T}}^{\mathrm{miss}}$ or $E_{\mathrm{T}}^{\mathrm{miss}}$ direction:
    (a) Gaussian core of the $E_{\mathrm{T}}^{\mathrm{miss}}$ resolution distribution.
    (b) Unusual or extreme mismeasurements that populate the tails of the $E_{\mathrm{T}}^{\mathrm{miss}}$ resolution distribution, especially those poorly predicted by the simulation.
3. The widths of the produced particles.
4. Presence of backgrounds containing τ leptons, which in leptonic decay cases can produce an isolated e or μ with additional neutrinos that spoil the M_{T2} shape.

Out of hand we may reject lepton resolution as the cause of the tail since the resolution for leptons is much better than for the other ingredients.

As a next step, we can try to determine to what extent (2a) and (2b) affect the M_{T2} distribution. Figure 12 is suggestive, see AN-12-268 for a full discussion. Note that, with all recommended MET filters applied there is essentially no MET tail beyond what is predicted by the simulation. While there are technical differences between the cleaning applied in Figure 12 and in this analysis, we should on average expect our selected events to have much better MET resolution than this more inclusive sample due to our requirement of two high-p_{T} leptons and two high-p_{T} jets.

We can estimate the effect of the Gaussian core of the resolution on the tail in M_{T2} with a study on simulation that compares M_{T2} calculated with reconstructed $E_{\mathrm{T}}^{\mathrm{miss}}$ to the same events calculated with generated $E_{\mathrm{T}}^{\mathrm{miss}}$ instead. What we find is summarized in Figure 13. We use $t\bar{t}$ simulated events to carry out the study as they determine the shape of the falling edge in data. First, we compute M_{T2} in the usual way for our events, using the reconstructed leptons and $E_{\mathrm{T}}^{\mathrm{miss}}$. We find the familiar M_{T2} falling edge shape. Next, we recompute it using the generator-level $E_{\mathrm{T}}^{\mathrm{miss}}$, representing the case where the resolution is perfect. We find that while the falling edge is shifted to the left (as you would expect compared to the finite resolution case), the tail does not disappear as is consistent with our understanding of its origin. To see how much of the tail shape can be explained by the Gaussian componenet of the resolution, we fit a simple Gaussian to the core of the $E_{\mathrm{T}}^{\mathrm{miss}}$ resolution plot for the selected sample and then re-smear the generator-level $E_{\mathrm{T}}^{\mathrm{miss}}$ by this resolution. The result is the gold curve. It matches the shape of the reconstructed $E_{\mathrm{T}}^{\mathrm{miss}}$ case very well. We interpret this result to mean that the Gaussian component of the $E_{\mathrm{T}}^{\mathrm{miss}}$ resolution is the primary determinant of the shape in this falling edge region.

We check for catastrophic failures of M_{T2} reconstruction (2b) in a b-vetoed control sample, leaving all other event selection criteria intact. The results of this check are shown in Figure 14. For M_{T2} cuts used in this analysis (at 80-120 GeV), the simulation slightly overpredicts the number of events above the cut value by a factor of 5% (80 GeV) to 20% (120 GeV) though the statistics of this sample are small enough that these deviations at large M_{T2} are not statistically significant. For the one event observed in data, it is worth noting that it falls just outside the Z-veto region (111 GeV) and that the angle between the Z candidate and the $E_{\mathrm{T}}^{\mathrm{miss}}$ vector is nearly

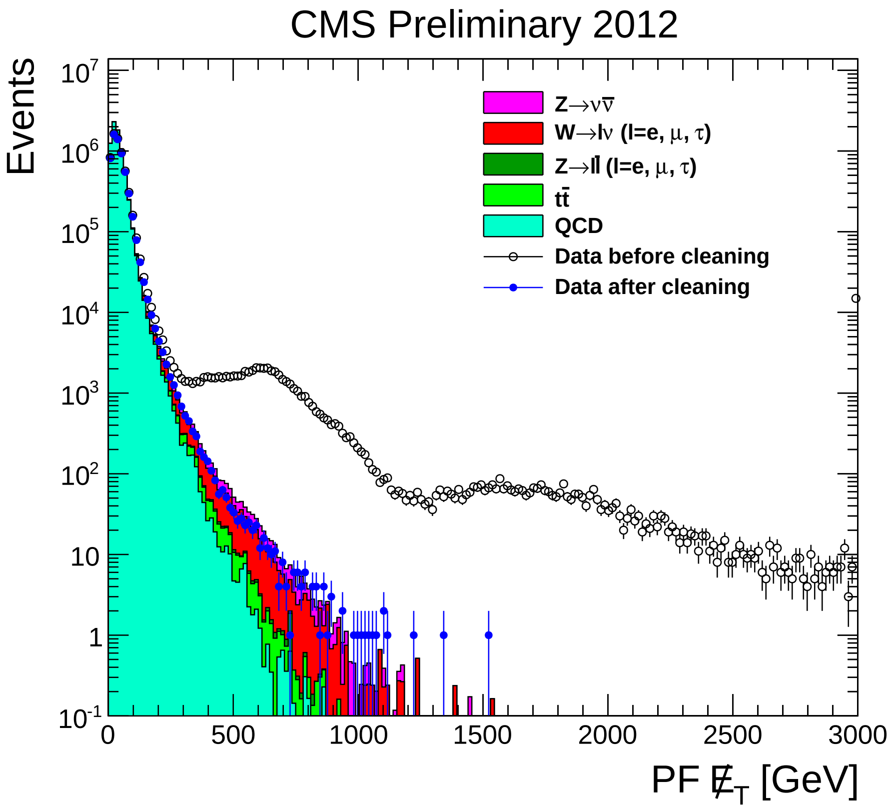

Figure 12: PFMET distributions for dijet events with no MET filters applied (black circle), with filters applied (blue dot). The filled histograms show different MC contributions [2].

back-to-back, indicating it is likely a Z event with mismeasured hadronic recoil. We conclude that there is no evidence for a population of high-M_{T2} events caused by unusual or extreme mismeasurements of $E_{\mathrm{T}}^{\mathrm{miss}}$.

The final sources of the tail, (3) and (4), can be evaluated with Figure 15. Here M_{T2} is evaluated purely at generator level, vetoing events with tau leptons. We see that the shape is virtually identical as before. The only effects determining the shape of this plot are the kinematics of the simulated events and the mass distribution of the Ws due to their finite width.

When the M_{T2} cut is low, the number of observed events above the cut is dominated by the shape of the falling edge and not the extreme tail. If the tail fell more or less sharply in data than in simulation, our simulation can predict too many or too few events in the signal region. We check for evidence of a mis-modeling in the $M_{T2} < 80$ GeV control region samples in order to put an upper limit on the size of the effect.

Our strategy revolves around the use of the $\Delta\phi$ between the dilepton system and the $E_{\mathrm{T}}^{\mathrm{miss}}$. By looking at the smallest angle configurations, we can look at the falling edge of the MT2 distribution while remaining blinded to the signal region. If there are sources of spurious high-M_{T2} events in data (due to additional backgrounds not considered in the analysis, mismeasurement of high $E_{\mathrm{T}}^{\mathrm{miss}}$ tails, or other unanticipated sources) we should expect to see an excess here. The fact that the existing systematics cover the observed values of M_{T2} in data suggests that no

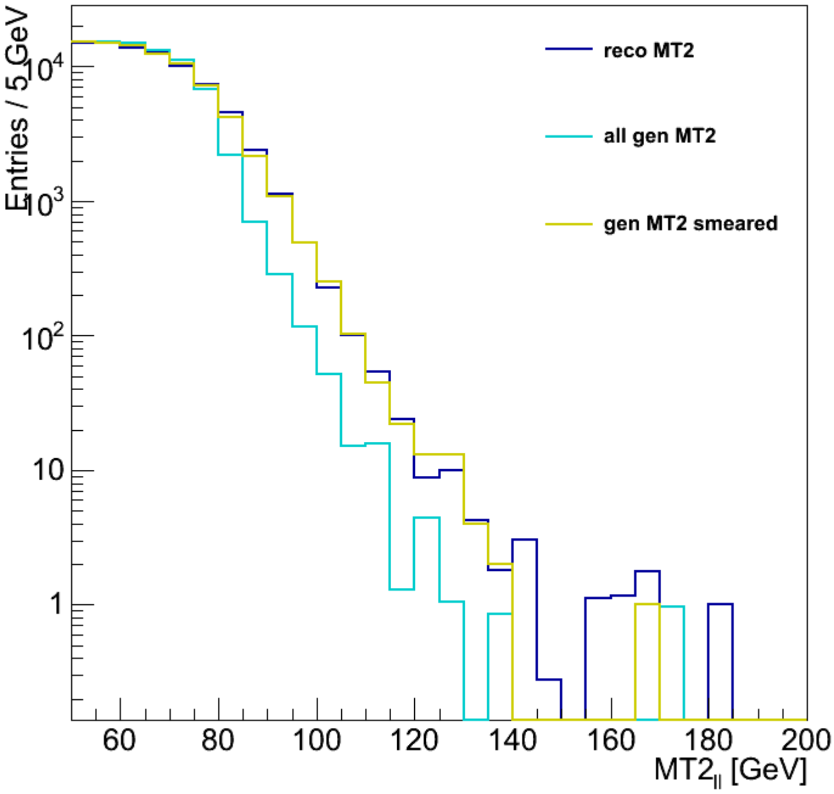

Figure 13: M_{T2} distribution for simulated $t\bar{t}$ in three different cases. In dark blue, the distribution is shown using reconstructed $E_{\mathrm{T}}^{\mathrm{miss}}$ as would be done for data events. In light blue, the same distribution in shown substituting generator-level $E_{\mathrm{T}}^{\mathrm{miss}}$ for reconstructed $E_{\mathrm{T}}^{\mathrm{miss}}$. In gold, we smear the generated $E_{\mathrm{T}}^{\mathrm{miss}}$ by the method indicated in the text, and recover essentially the same result as for reconstructed $E_{\mathrm{T}}^{\mathrm{miss}}$.

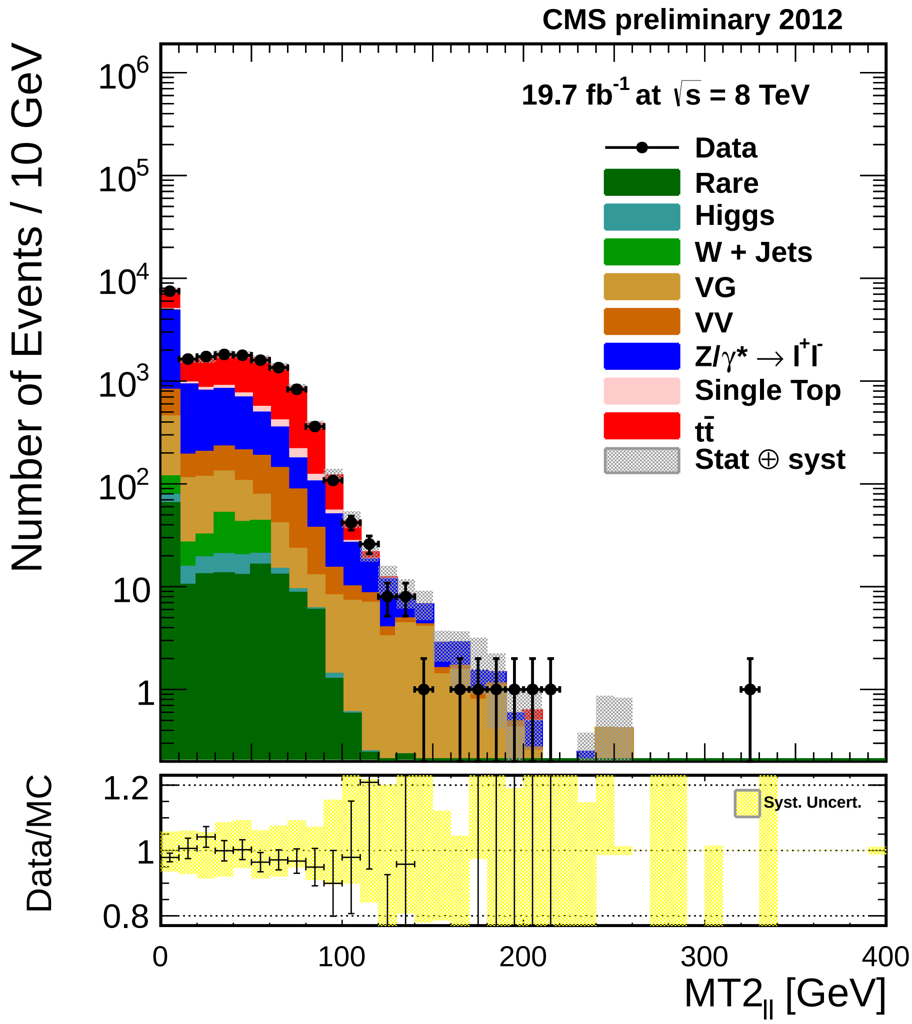

Figure 14: M_{T2} distribution for the b-veto control sample.

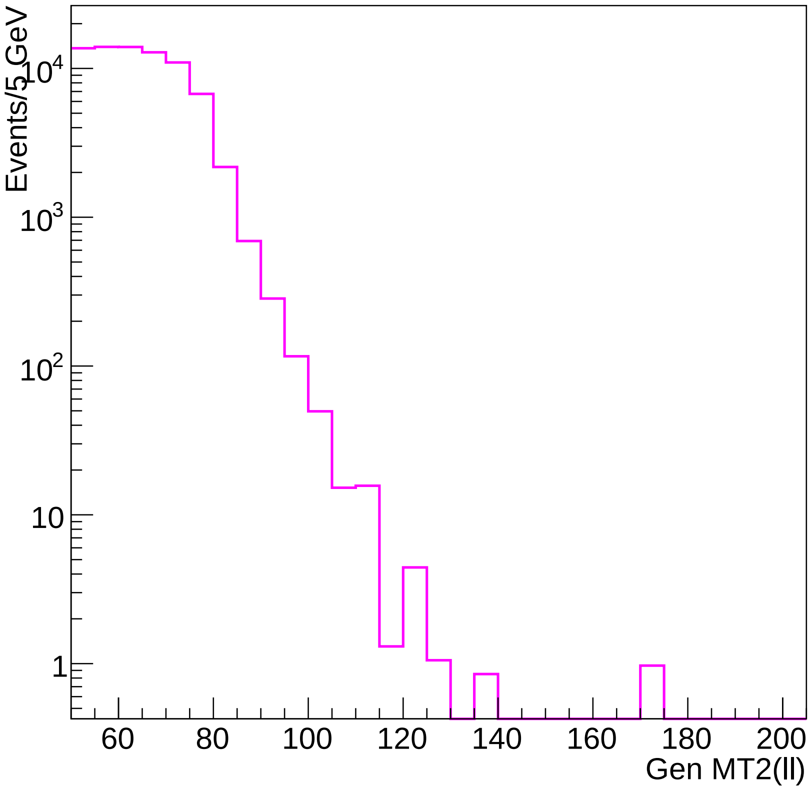

Figure 15: M_{T2} distribution for simulated $t\bar{t}$ at generator level. Events containing τ leptons are also vetoed, so the resulting M_{T2} distribution contains only the effects of the event kinematics and the width of the produced particles.

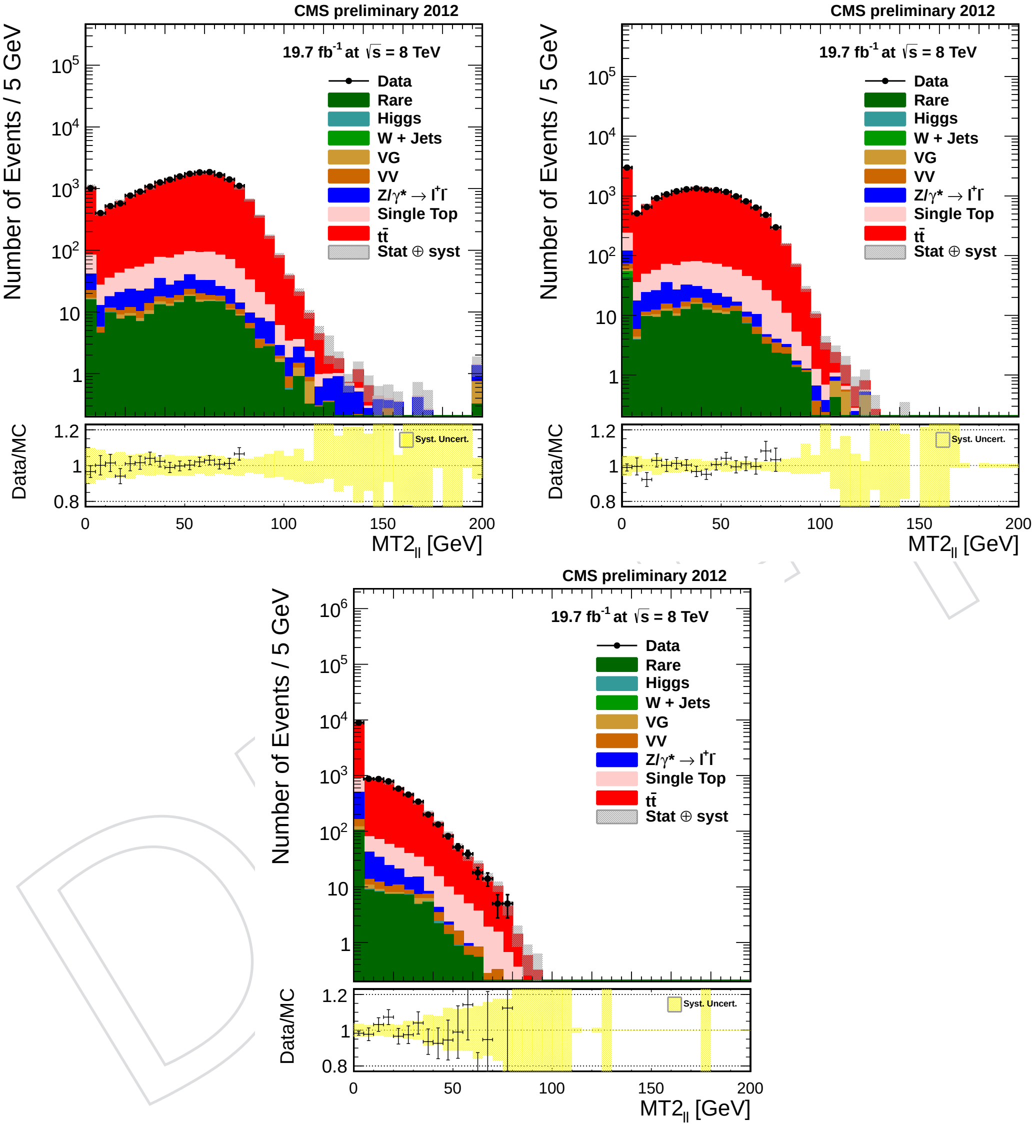

Figure 16: Comparison of M_{T2} shapes for data and simulation. The three plots are for different bins of $\Delta\phi(ll, E_{\mathrm{T}}^{\mathrm{miss}})$: $\Delta\phi > 2\pi/3, \pi/3 < \Delta\phi < 2\pi/3, \Delta\phi < \pi/3$ respectively. The existing systematics are sufficient to cover any differences in the modeling of the falling edge of the M_{T2} distribution.

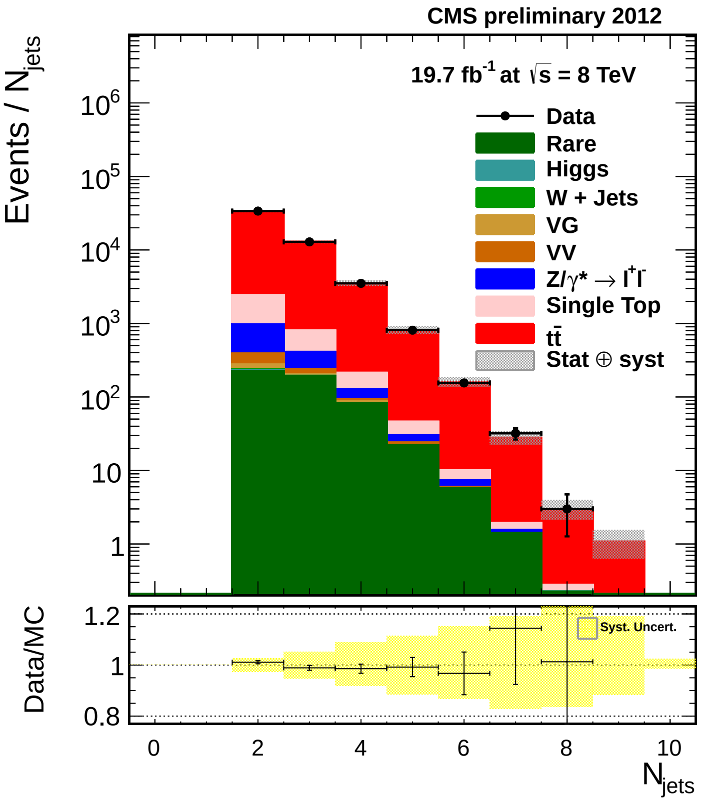

Figure 17: Number of jets passing the jet identification requirement in events passing the full event selection. The number of jets in simulation and data are in good agreement for up to eight jets in the final state, which is the highest multiplicity observed in our selected data sample. The full suite of systematic uncertainties is applied to the simulation.

such effects are present in our selected sample.

To summarize the results of the M_{T2} shape analysis:

- The shape of the falling edge is primarily motivated by the width of the W.
- The smearing of the shape due to E_T^{miss} mismeasurements can be well approximated using only the Gaussian core of the E_T^{miss} response in simulation, suggesting that unusually large mismeasurements play only a minor role.
- Control samples in data can be used to establish that both the shape of the falling edge and the number of events in the far tails are well predicted by simulation compared to the known systematic uncertainties.

As a result, we do not apply any additional systematic for the M_{T2} shape.

5.1 Cross checks on modeling of object multiplicities and event kinematics

Since we use simulation to estimate the number of background events in the signal region, this section presents a number of checks on the modeling of object multiplicities and event kinematics in the simulation samples. Overall, when comparing the simulated prediction with the data in the control regions, we find good to excellent agreement between the two.

The modeling of the number of jets in the selected events is shown in Figure 17. If the jet multiplicity distribution was poorly modeled by the simulation, we would see its effects in the number of events passing the event selection, and there would be further effects on the

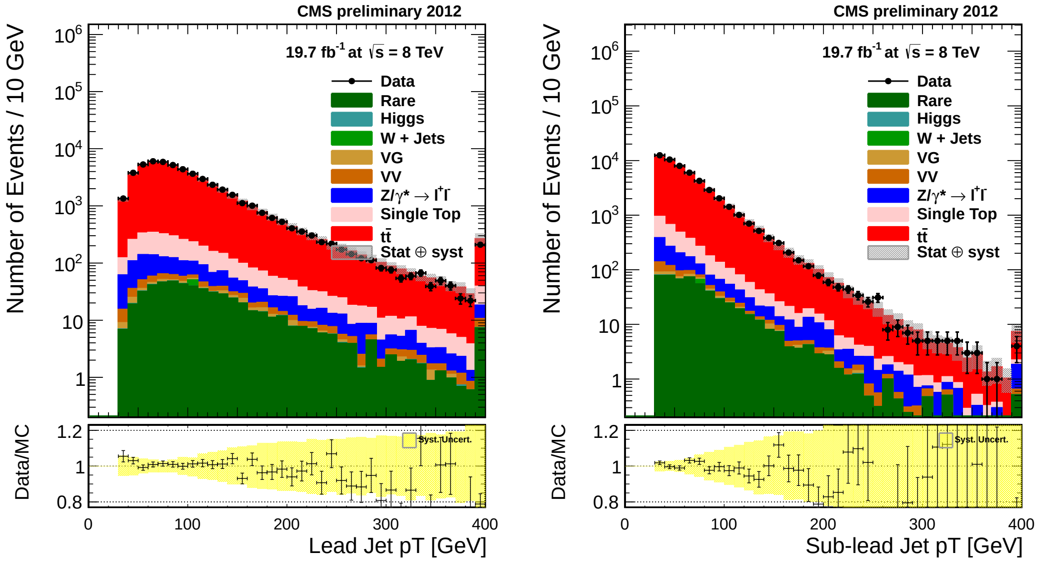

Figure 18: Jet p_T for the leading (left) and lagging (right) jet in events passing the full selection. Good agreement is seen across the whole range of p_T relevant to the analysis.

modeling of the E_T^{miss} and therefore M_{T2}. We see good agreement between the jet multiplicity distributions in simulation and data.

The p_T of the leading and lagging jet in selected events are shown in Figure 18. The jet p_T directly affects the efficiency of the jet p_T selection and has an indirect effect on the modeling of E_T^{miss} and therefore also M_{T2}. We see good agreement across the whole range of jet p_T relevant to the analysis.

The b-tagged jet multiplicity is shown in Figure 19. If the b-tagging efficiency was not well modeled in the simulation, we would expect to obtain the wrong selection efficiency for both data and simulation. When plotted against the simulation using only the b-tagging efficiency scale factor uncertainty, we see good agreement between the two distributions. The existing systematic uncertainty on the b-tagging efficiency is sufficient for even three or four b-jets in the final state.

The p_T of the leading and lagging b-tagged jet are shown in Figure 20. Since the majority of b jets in the selected sample come from the decay of top quarks, a difference between data and simulation for this observable can indicate problems with the simulation of the kinematics of the $t\bar{t}$ system. Since we obtain good agreement over the relevant range of p_T we conclude that no such problems are present in our selected sample.

The p_T of the leading and lagging leptons in selected events are shown in Figure 21. The p_T of the leptons affects not only the efficiency of the lepton selection but is also one of the inputs to M_{T2}. Good agreement is seen over the whole range of lepton p_T.

The p_T of the dilepton system is shown in Figure 22. The p_T of the dilepton system is related to M_{T2}. Good agreement can be seen over the whole range of dilepton system p_T.

6 Results

Table 19 shows the background predictions of Table 14 along with the observed number of events in the unblinded signal region in data.

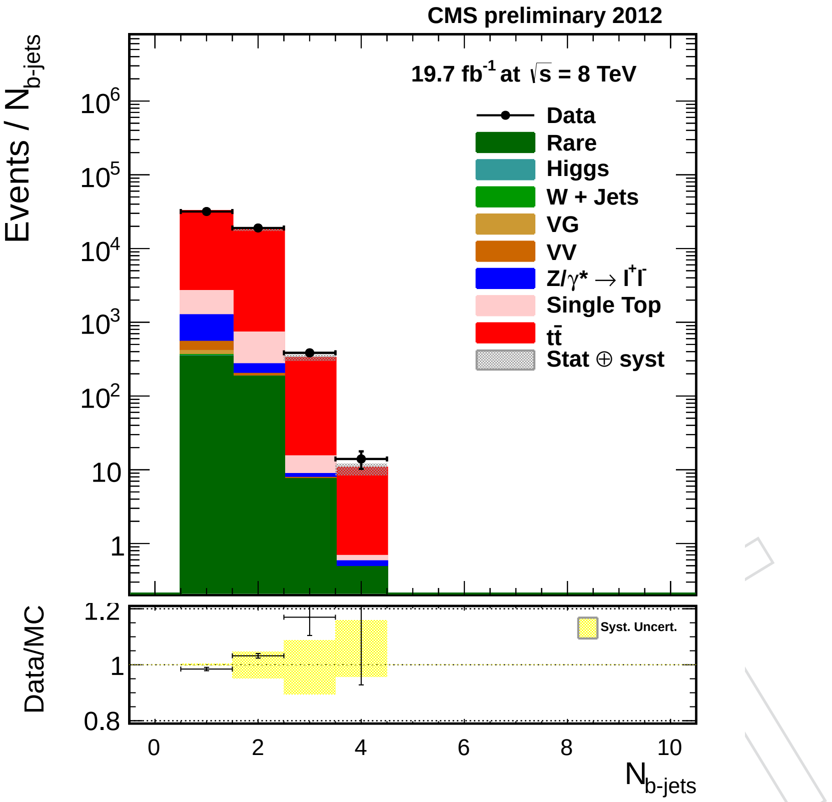

Figure 19: Number of b-tagged jets in events passing the full event selection. The number of b-tagged jets are in good agreement for up to four b-tagged jets in the final state. The systematic uncertainty shown is only on the b-tagging effeciency scale factor.

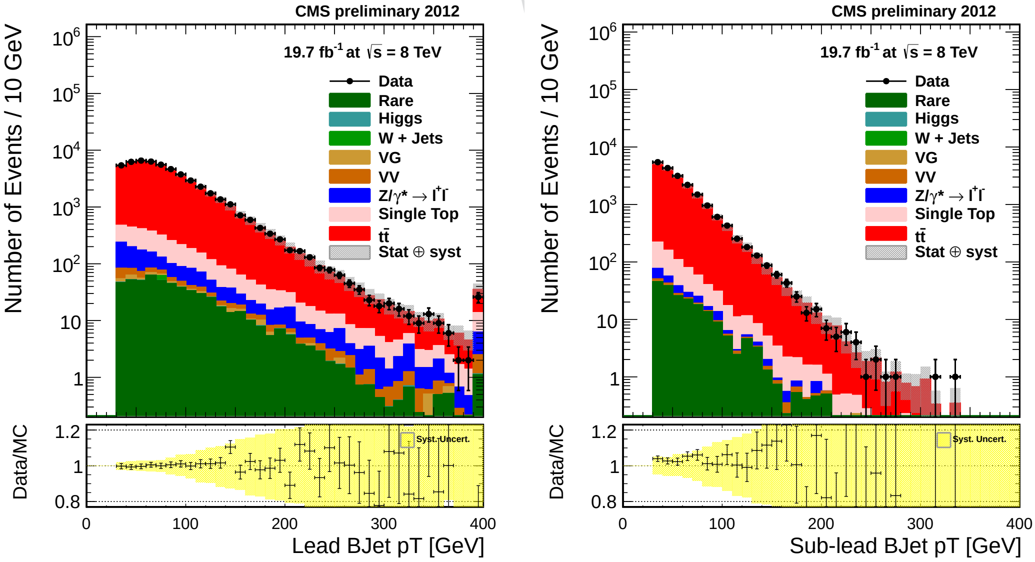

Figure 20: b-tagged jet p_T for the leading (left) and lagging (right) selected b-tagged jet. Agreement between data and simulation is good over the whole range of p_T relevant to the analysis.

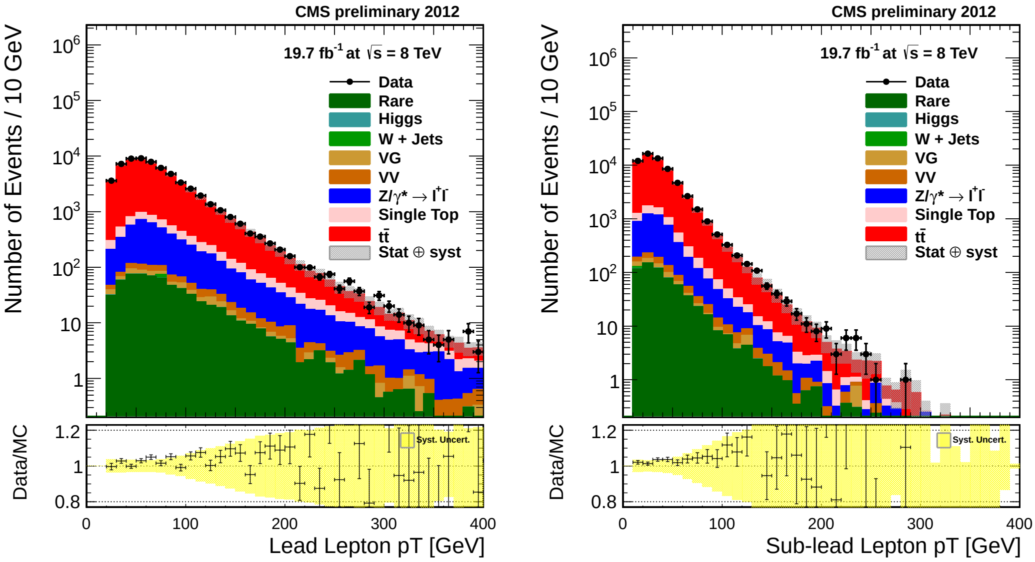

Figure 21: p_T distribution for selected leptons, leading (left) and lagging (right). Good agreement is seen over the whole range of lepton p_T.

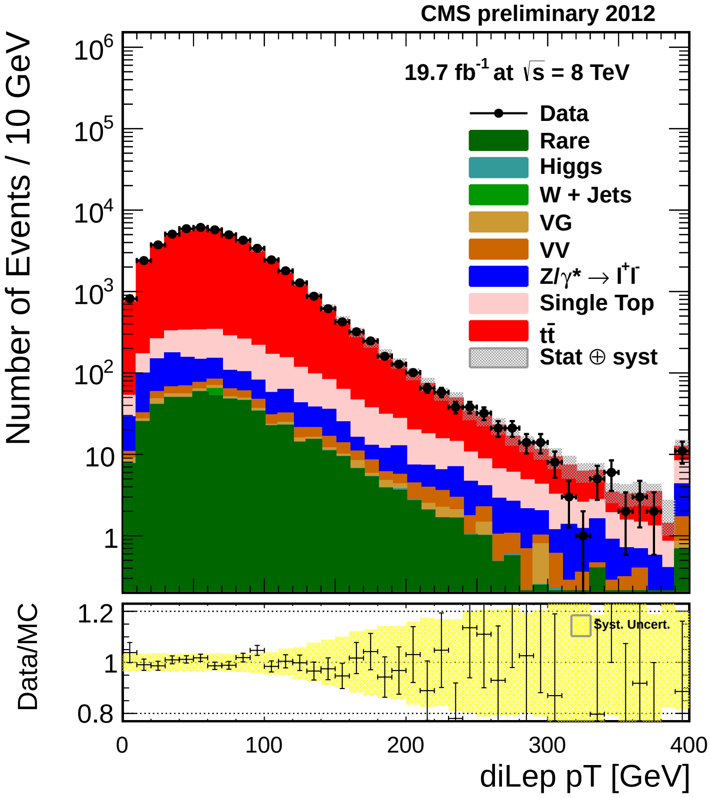

Figure 22: p_T of the dilepton system in selected events. Good agreement can be seen over the whole range of dilepton system p_T.

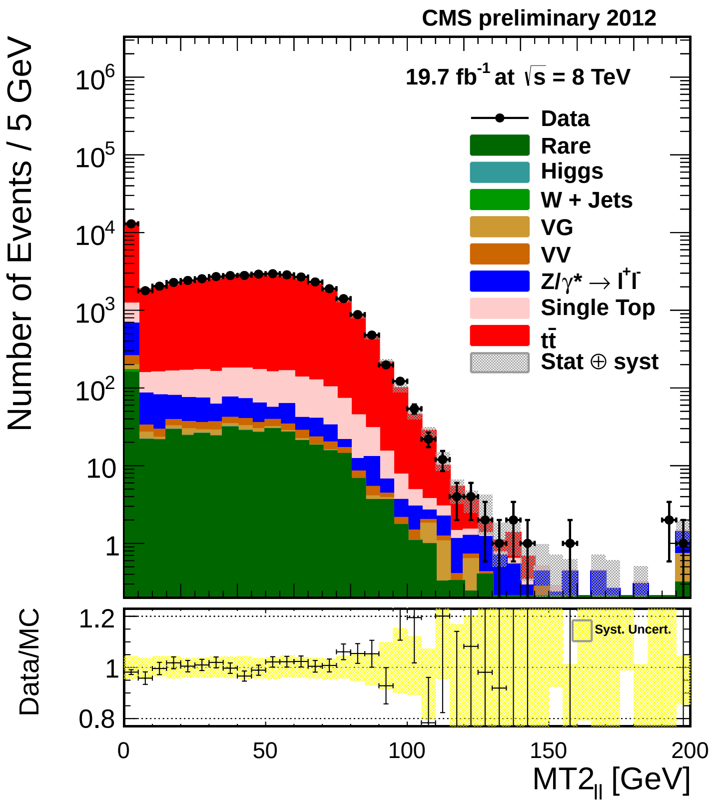

Figure 23: Full unblinded M_{T2} distribution with full systematics.

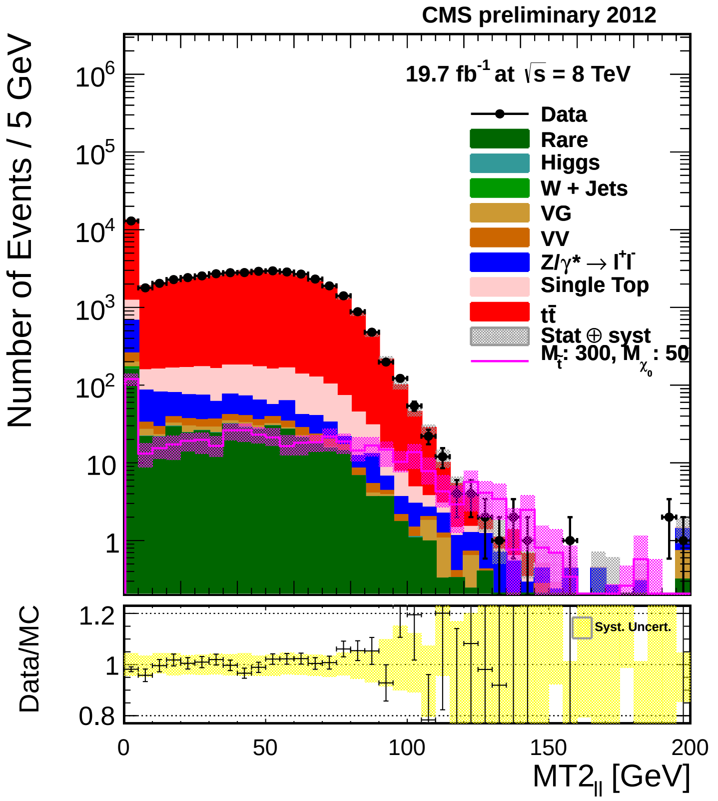

Figure 24: Full unblinded M_{T2} distribution with full systematics. For comparison, a T2tt model point with 300 GeV stop and 50 GeV LSP is shown in magenta.

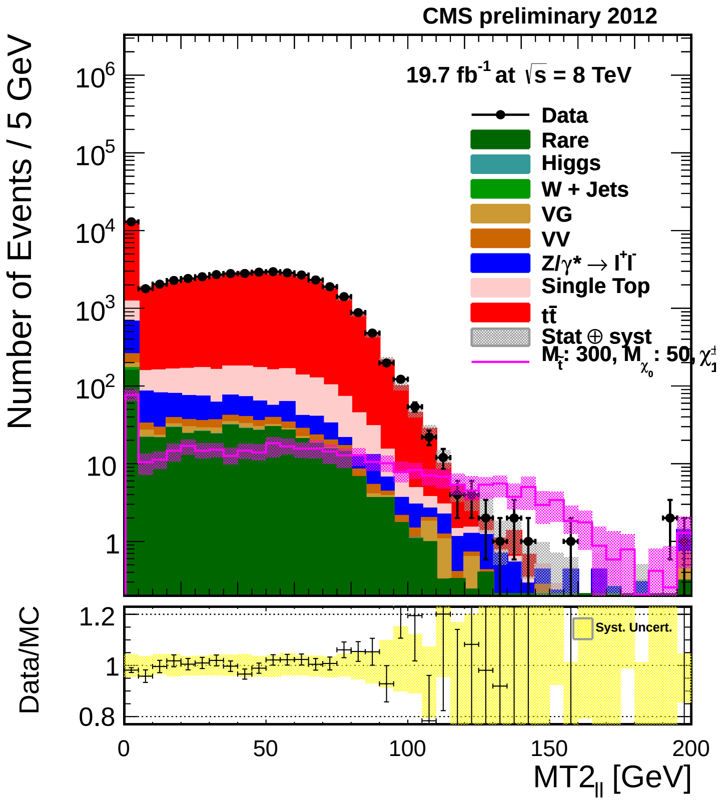

Figure 25: Full unblinded M_{T2} distribution with full systematics. For comparison, a T2bw model point with 300 GeV stop, 50 GeV LSP, and 190 GeV chargino is shown in magenta.

Figure 23 shows the full unblinded M_{T2} distribution. Figures 24 and 25 show the same distribution with example signal models for $M_{stop} = 300$ GeV. The agreement between data and the backgound prediction in the signal region is excellent in all cases. Since we observe no excess over the SM background we proceed to set limits.

6.1 Examination of data events with high M_{T2}

We chose three events in data with M_{T2} greater than 190 GeV to examine in detail, as a cross-check in case the large observed value was due to unexpected detector effects or reconstruction failures. NB that the number of high M_{T2} events is predicted with good accuracy by the simulation, so we expect to find mostly genuine physics events where well-understood detector acceptance or resolution effects have introduced spuriously high $E_{\mathrm{T}}^{\mathrm{miss}}$ values.

The first event is shown in Figure 26. The M_{T2} for this event is 190 GeV. It is a $\mu\mu$ event containing six jets above 50 GeV. The large value of M_{T2} comes from the $E_{\mathrm{T}}^{\mathrm{miss}}$ pointing opposite to the high p_{T} $\mu\mu$ system. The mass of the dilepton system is 43 GeV, the $E_{\mathrm{T}}^{\mathrm{miss}}$ is 140 GeV, and the angle between them is 2.7 radians. The $E_{\mathrm{T}}^{\mathrm{miss}}$ points near a high (180 GeV) p_{T} jet which is almost perfectly back-to-back with the dilepton system. One possible explanation for this event is that this recoiling jet is badly mismeasured. Close inspection of the objects in the event did not reveal any irregularities.

The second event is shown in Figure 27. The M_{T2} for this event is also 190 GeV. It is a $\mu\mu$ event with three jets above 50 GeV. Again, the $E_{\mathrm{T}}^{\mathrm{miss}}$ points opposite to the high p_{T} $\mu\mu$ system. The mass of the dilepton system is 75 GeV, falling just outside the Z veto window which starts at 76 GeV. The $E_{\mathrm{T}}^{\mathrm{miss}}$ is 100 GeV and the angle between the leptons and the $E_{\mathrm{T}}^{\mathrm{miss}}$ is 2.9 radians.

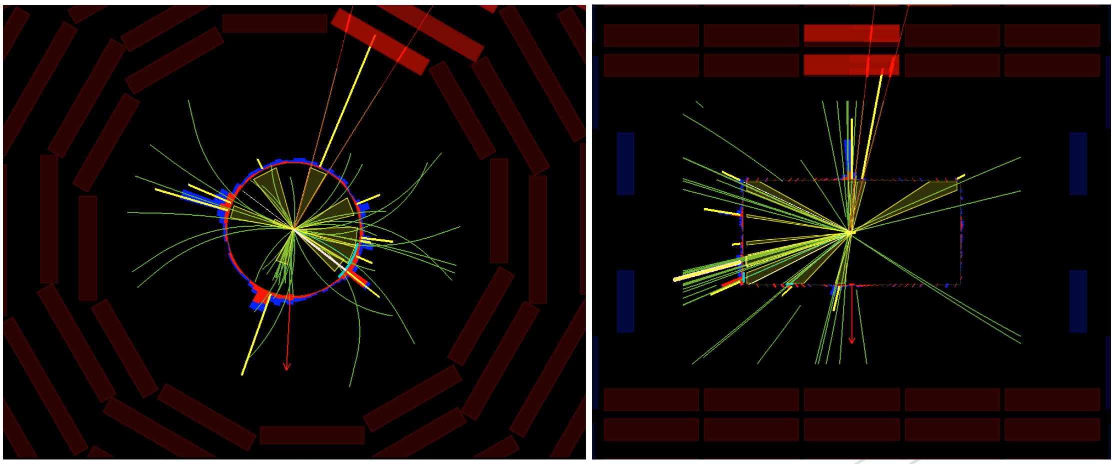

Figure 26: High-M_{T2} $\mu\mu$ event number 1.

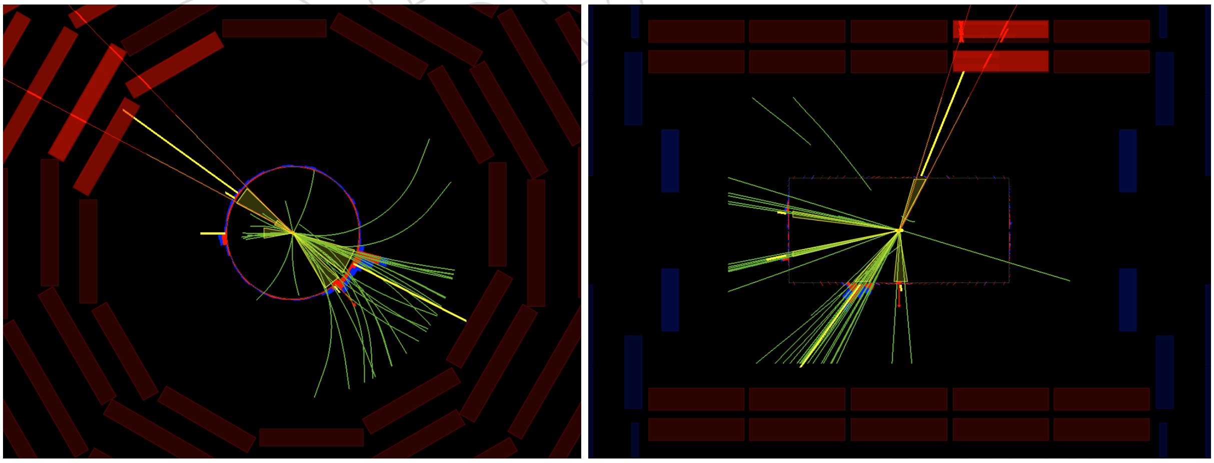

Figure 27: High-M_{T2} $\mu\mu$ event number 2.

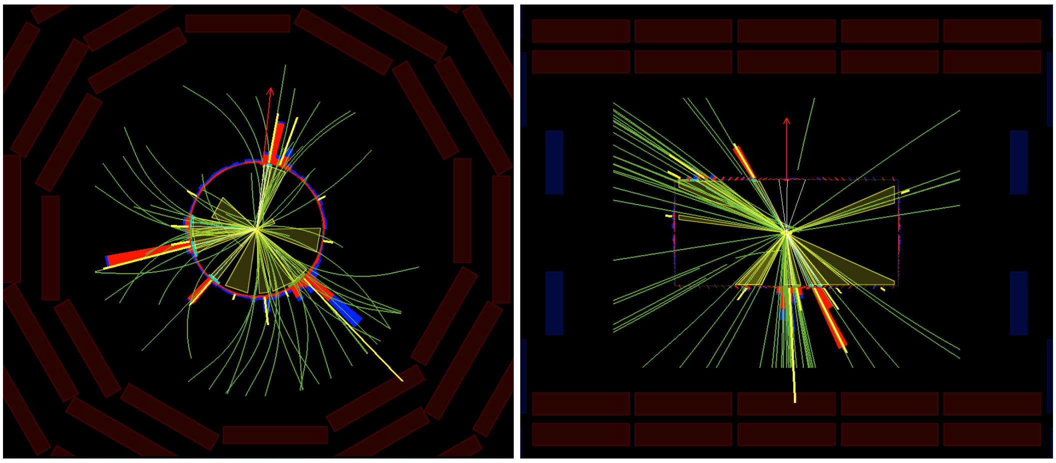

Figure 28: High-M_{T2} ee event number 3.

Likely this is a $Z \to \mu\mu$ event where the hadronic recoil is mismeasured.

The third event is shown in Figure 28. It is an ee event, but the electrons (in cyan) are not easily seen due to the large multiplicity of high p_{T} particles in this event. The M_{T2} for this event is about 270 GeV, a remarkable value. The event had an extremely large amount of activity with seven jets above 50 GeV. The invariant mass of the electron pair is 106.3 GeV, falling just above the Z veto window which ends at 106 GeV. The $E_{\mathrm{T}}^{\mathrm{miss}}$ is aligned near two of the high p_{T} recoiling jets, so it is likely that this is a $Z \to ee$ event where the hadronic recoil is mismeasured.

NB that all three events are same-flavor as anticipated by the simulation, as high-multiplicity $Z + X$ events contribute to the tails much more in same-flavor channels.

7 Limit setting

The theoretical prediction for the stop cross section used for the limit calculation is shown in Figure 29. The same cross section for stop production is used regardless of the decay mode considered.

The acceptance for each point is derived from the simulation as shown in Figure 30. For each point, we use the cut on M_{T2} which gives the best expected limit on the signal strength given the yields in simulation. Cut values between 80 and 140 GeV were tested in steps on 10 GeV, but for T2tt, cuts above 120 GeV never give the best limit due to very small signal efficiency. Lower cuts (80 to 90 GeV) give some sensitivity in the region where the top decay is off-shell, as shown in Figure 31. The same procedure for establishing the systematic uncertainty in the background yield is used at each signal point to derive a systematic uncertainty on the signal acceptance at that point. In addition to the uncertainties on background we include an additional term for the uncertainty in the stop cross section at NLO as computed by the LPCC SUSY cross section working group.

Expected limits for the T2tt SMS in the (stop mass, neutralino mass) plane are shown in Figure 32. (NB that these limits are computed with the asymptotic setting of the Higgs Combine tool for now, we will do the full computation once things are more stable.)

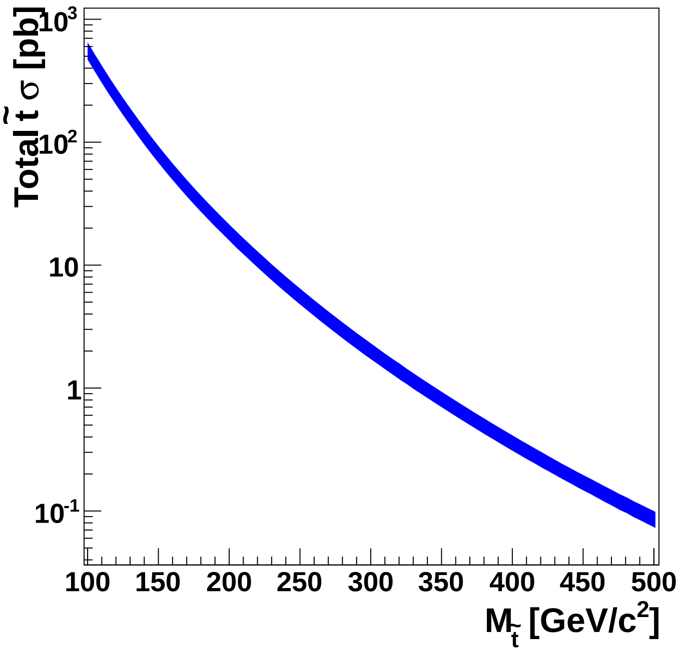

Figure 29: Stop cross section as a function of mass as used in the limit setting. The blue band indicates the systematic uncertainty on the stop cross section.

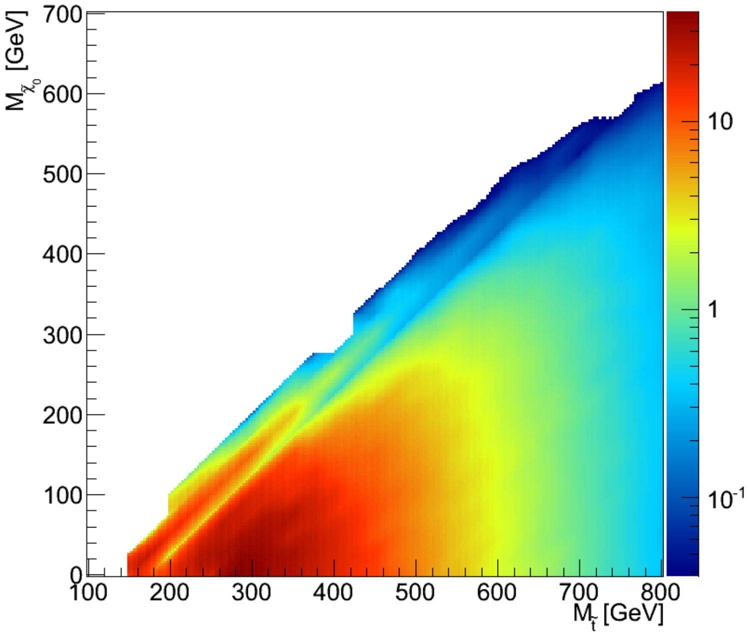

Figure 30: Signal yield of the selection for the T2tt SMS with a cut of 110 GeV on M_{T2} for the integrated luminosity used in this analysis. The diagonal feature that intersects the x-axis at the top mass corresponds to model points for which the mass splitting between the stop and χ^0 is equal to the top mass. Points above the line therefore have off-shell top decays.

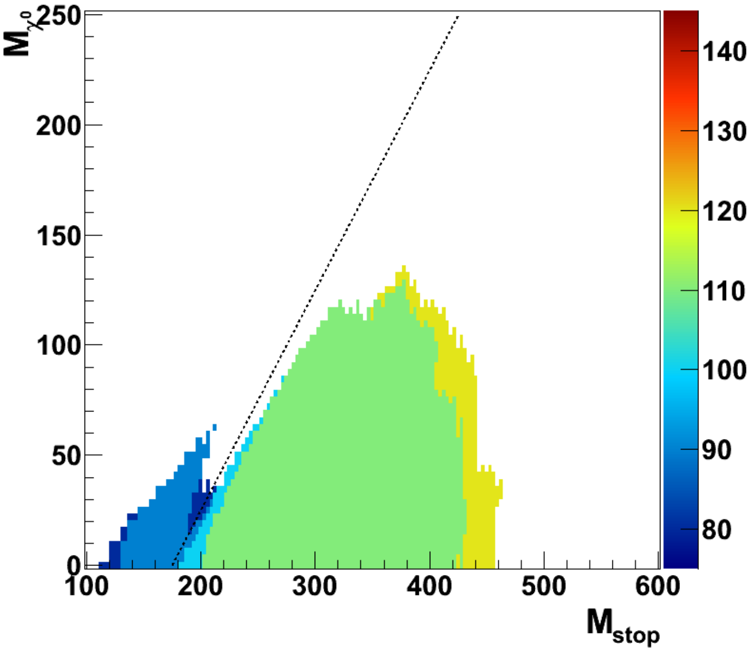

Figure 31: Output of the optimiztion of M_{T2} cut for the T2tt signal model. The dotted line indicates the model points for which the mass splitting between the stop and χ^0 is equal to the top mass. The z-axis shows which cut value gives the best expected limit on the signal strength. Points inaccessible for this analysis strategy are left uncolored.

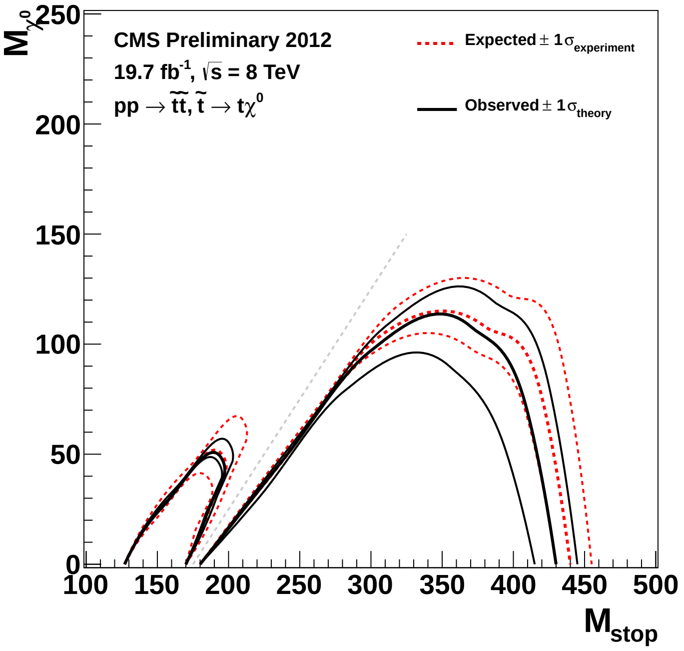

Figure 32: 95% CL expected limits for the T2tt SMS in the stop mass, neutralino mass plane. The median expected limit is in yellow while the positive and negative one-σ expected limits are shown in blue and red.

References

[1] C. G. Lester and D. J. Summers, “Measuring masses of semiinvisibly decaying particles pair produced at hadron colliders”, *Phys. Lett.* **B463** (1999) 99–103, `doi:10.1016/S0370-2693(99)00945-4`, `arXiv:hep-ph/9906349`.

[2] Liu, Hongxuan et al., “Fake missing transverse momentum in the 2012 data set”,.

channel	ϵ_{data}	ϵ_{MC}	SF
ee	0.949 ± 0.003	0.879 ± 0.001	1.080 ± 0.011
$\mu\mu$	0.948 ± 0.001	0.966 ± 0.001	0.981 ± 0.010
$e\mu$	0.918 ± 0.002	0.911 ± 0.001	1.008 ± 0.010

Table 16: Global trigger efficiencies ϵ for data and MC and resulting scale factors derived for the **stop FastSim** sample. The scale factors include 1% systematic uncertainty in addition to statistical uncertainties from MC and data.

channel	ϵ_{data}	ϵ_{MC}	SF
ee	0.949 ± 0.003	0.938 ± 0.003	1.011 ± 0.011
$\mu\mu$	0.948 ± 0.001	0.969 ± 0.003	0.978 ± 0.010
$e\mu$	0.918 ± 0.002	0.941 ± 0.003	0.976 ± 0.011

Table 17: Global trigger efficiencies ϵ for data and MC and resulting scale factors derived for the $\mathrm{t\bar{t}}$ **background** sample. The scale factors include 1% systematic uncertainty in addition to statistical uncertainties from MC and data.

	Eff Data	Eff. FullSim	SF FullSim	Eff. FastSim	SF FastSim
Muon	0.9361±0.0001	0.9452±0.0001	0.9904±0.0002	0.9715±0.0001	0.9636±0.0002
Electron	0.7871±0.0002	0.8114±0.0002	0.9701±0.0002	0.8452±0.0002	0.9312±0.0002

Table 18: Muon and electron identification and isolation efficiencies, measured in data and with the Drell-Yan samples (full and fast simulation. The errors correspond only to the statistical uncertainty.

M_{T2} value	Data	Expected bkg.	Stat. unc.	Sys. unc.	
80	1784	1702.4	17.2	+110.6	-113.1
90	426	414.0	8.2	+44.0	-38.8
100	106	101.5	3.9	+11.5	-12.7
110	30	28.2	2.0	+7.1	-2.4
120	14	12.9	1.2	+3.4	-1.4

Table 19: Data yields and background expectation for five different M_{T2} cut values.